The Astrophysical Journal, 903:44 (28pp), 2020 November 1 https://doi.org/10.3847/1538-4357/abb950

The Extreme Red Excess in Blazar Ultraviolet Broad Emission Lines

Brian Punsly[1,2], Paola Marziani[3], Marco Berton[4,5], and Preeti Kharb[6]
[1] 1415 Granvia Altamira, Palos Verdes Estates, CA 90274, USA ; brian.punsly@cox.net
[2] ICRANet, Piazza della Repubblica 10 Pescara 65100, Italy and ICRA, Physics Department, University La Sapienza, Roma, Italy
[3] INAF, Osservatorio Astronomico di Padova, Italy
[4] Finnish Centre for Astronomy with ESO (FINCA), University of Turku, Vesilinnantie 5, FI-20014, University of Turku, Finland
[5] Aalto University Metsähovi Radio Observatory, Metsähovintie 114, FI-02540 Kylmälä, Finland
[6] National Centre for Radio Astrophysics - Tata Institute of Fundamental Research, S. P. Pune University Campus, Ganeshkhind, Pune 411007, India
Received 2020 August 15; revised 2020 September 9; accepted 2020 September 10; published 2020 October 30

Abstract

We present a study of quasars with very redward asymmetric (RA) ultraviolet (UV) broad emission lines (BELs). An excess of redshifted emission has been previously shown to occur in the BELs of radio-loud quasars and is most extreme in certain blazars. Paradoxically, blazars are objects that are characterized by a highly relativistic blueshifted outflow toward Earth. We show that the red emitting gas resides in a very broad component (VBC) that is typical of Population B quasars that are defined by a wide Hβ BEL profile. Empirically, we find that RA BEL blazars have both low Eddington rates ($\lesssim$1%) and an inordinately large (order unity) ratio of long-term time-averaged jet power to accretion luminosity. The latter circumstance has been previously shown to be associated with a depressed extreme UV ionizing continuum. Both properties conspire to produce a low flux of ionizing photons, two orders of magnitude less than typical Population B quasars. We use CLOUDY models to demonstrate that a weak ionizing flux is required for gas near the central black hole to be optimally ionized to radiate BELs with high efficiency (most quasars overionize nearby gas, resulting in low radiative efficiency). The large gravitational redshift and transverse Doppler shift result in a VBC that is redshifted by $\sim$2000–5000 km s^{-1} with a correspondingly large line width. The RA BELs result from an enhanced efficiency (relative to typical Population B quasars) to produce a luminous, redshifted VBC near the central black hole.

Unified Astronomy Thesaurus concepts: Quasars (1319)

1. Introduction

Quasars are characterized by bright broadband emission from a galactic nucleus with a spectral energy distribution (SED) that peaks in the ultraviolet (UV). This bright quasi-stellar emission is considered to arise from viscous dissipation from an accretion flow onto a supermassive black hole (Malkan 1983). Furthermore, quasar optical/UV spectra typically contain luminous broad emission lines (BELs). The quasar broadband continuum and the BELs offer clues to the state of the accreting gas. Another prominent feature occurs in $\sim$10% of quasars. These quasars possess powerful relativistic radio jets and are known as radio-loud quasars (RLQs). The preponderance of quasars have weak or absent radio jets and are known as radio-quiet quasars (RQQs). Surprisingly, despite the on or off condition for the extremely powerful jet, there are no conspicuous differences between the observed signatures of the accretion states in RLQs and RQQs. To first order, the continua and BELs in RLQS and RQQs are remarkably similar (Corbin & Francis 1994; Zheng et al. 1997; Richards et al. 2002; Telfer et al. 2002). Systematic differences in the two families of spectra are only revealed by the study of subtle lower-order spectral features (Corbin 1997b; Telfer et al. 2002; Punsly 2014). Consequently, the difference between the black hole accretion system (the putative central engine) is still poorly constrained by observation, and therefore so is our understanding of the dynamics of relativistic jet launching more than 50 yr after their discovery in quasars.

This similarity of accretion signatures is perplexing from a theoretical point of view. Numerical models of the accretion have offered little, if any, insight into the subtle spectral difference. From a continuum point of view, the first difference that has been found involves the extreme-ultraviolet (EUV) tail of the spectral energy distribution (Zheng et al. 1997; Telfer et al. 2002). RLQs have a deficit of EUV emission (the EUV deficit) relative to RQQs, and the degree of this deficit increases with the relative strength of the long-term time-averaged jet power, $\overline{Q}$, compared to the accretion flow bolometric luminosity, $L_{\rm bol}$ (Punsly 2015). Namely, the magnitude of the EUV luminosity below 1100 Å relative to the SED peak luminosity at $\sim$1100 Å is anticorrelated with $\overline{Q}/L_{\rm bol}$.

In this paper, we concentrate on the most conspicuous difference seen in the BELs between RLQs and RQQs in order to see whether there are more clues to the difference in the accretion state or nuclear environment. The difference in line shapes between RQQ and RLQ BELs was summarized in Wills & Brotherton (1995): "The C IV BEL generally has stronger red than blue wings in RLQs, but the blue wing is often stronger than the red in RQQs. The Hβ BEL also often has stronger red wings in RLQs, with the RQQs showing similar frequency of red and blue asymmetries." The difference in the high-ionization C IV BEL was later quantified. There is a highly significant correlation between the spectral index from 10 GHz to 1350 Å and the amount of excess luminosity in the red wing of quasar C IV BELs, at >99.9999% statistical significance (Punsly 2010). The prominence of the redward excess is apparently associated with the radio jet emission mechanism and is most pronounced for lines of sight close to the jet axis.

In order to explore this strange occurrence of an excess of red emission in sources in which the plasma is beamed toward Earth, we look at the most extreme blazar red-winged BELs in detail. We also consider these sources in the context of complete samples of blazars. In order to construct a large sample, we need a UV line that is easily accessible and has

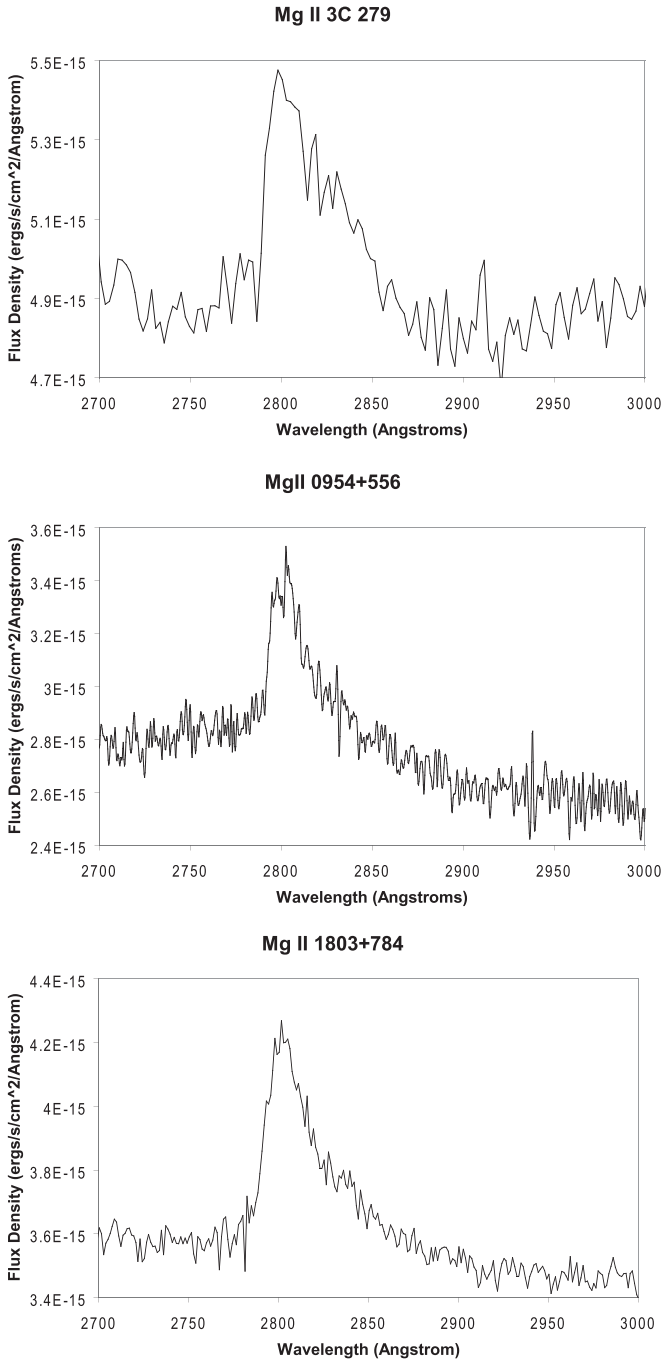

Figure 1. Extremely RA Mg II BELs of the three HPQs, 3C 279 (4/9/1992), 0954+556 (3/24/2012), and 1803+784 (07/04/1986). The flux densities are evaluated in the quasar rest frame.

been observed for entire samples of quasars that qualify as extreme blazars (objects that display extreme blazar properties as formally defined in Section 4). The only suitable line is Mg II λ2798 in spite of the difficulty of extracting the Fe II emission. There are three very redward asymmetric (RA) examples of an Mg II BEL, 3C 279 ($z = 0.536$), 0954+556 ($z = 0.899$, 4C +55.17) and S5 1803+784 ($z = 0.684$). They are very high polarization quasars (HPQs) that have been detected with $\sim$10% optical polarization (Impey & Tapia 1990; Lister et al. 2016). The Mg II profiles are shown in Figure 1 in order to demonstrate the extreme circumstance under consideration. This is not a subtle effect, nor a consequence of Fe II multiplets. The preponderance of the line shape is redshifted emission from, ostensibly, receding gas even though these objects have powerful jets relativistic of plasma beamed toward Earth. The motivation of this paper is that this is not coincidental. We surmise that even though the BEL gas is far from the central engine, there is valuable evidence on the nature of the accretion flow in RLQs that can be gleaned from this paradoxical circumstance.

In Section 2, we explore the BELs of four HPQs in detail: the three extreme RA blazars, 3C 279, 0954+556, and S5 1803 +784, and 3C 345, which has recently developed a significant redward asymmetry. The Mg II line is used to compare these sources to complete samples of extreme blazars. However, we also have C IV and Hβ lines that we consider as well for these quasars. In Section 3 and the Appendix, we introduce new radio images in order to define estimates of the long-term time-averaged jet power, $\overline{Q}$. Section 4 is a comparison of these sources to larger complete samples in order to see what makes them different from other extreme blazars. In the next section, we interpret the difference as a very low Eddington rate for a quasar and a very strong jet. In Section 6, we explore the effect of the polar line of sight on central black hole mass estimates and the inferred Eddington rate. Section 7 is a computation of the gravitational and transverse Doppler shift of a Keplerian disk of gas. In Section 8, we describe the ionization state resulting from a low Eddington rate combined with the EUV deficit associated with a strong jet. This motivates a CLOUDY analysis that compares the blazars with the RA BELs to conventional quasars and low Eddington rate Seyfert galaxies. The weak ionizing continuum seems to explain why these particular blazars have such large red asymmetries in their BEL profiles. We compare our explanation of highly RA UV BELs to other explanations that have been posited in the literature or might be possible in Section 10.

2. Blazars with Extreme RA Broad Emission-line Profiles

3C 279, 0954+556, and 1803+784 have very extreme blazar properties as are indicated in Table 1. Other extreme blazars are tabulated as well for future reference in Section 4. All three have a very high optical polarization. Both 3C 279 and 1803+784 are extremely superluminal. No component motion between epochs has been analyzed for 0954+556. All three are part of the Ghisellini et al. (2010) bright gamma-ray blazar sample. All of this is indicative of an outflow with very large Lorentz factors with a velocity vector aligned to within a few degrees of the line of sight, resulting in large Doppler enhancement (Lind & Blandford 1985).

The quasars 3C 279 and 0954+556 have the largest redward asymmetry, A (defined in Equation (1)), of the C IV BEL in the sample of Hubble Space Telescope (HST) spectra from the Evans and Koratkar Atlas of Hubble Space Telescope Faint Object Spectrograph Spectra of Active Galactic Nuclei and Quasars (Evans & Koratkar 2004; Punsly 2010). The quantity A is defined in terms of the FWHM, in Å, the midpoint of an imaginary line connecting a point defined at $1/4$ of the peak flux density of the BEL on the red side of the BEL to $1/4$ of the peak flux density on the blue side of the BEL, λ_{25}, and a similar midpoint defined at $8/10$ of the flux density maximum, λ_{80}, as

$$A = \frac{\lambda_{25} - \lambda_{80}}{\text{FWHM}}. \quad (1)$$

Table 1
Broad-line Blazar Properties

Quasar	Median Optical Polarization (%) Wills et al. (1992)	Jet Component Speed MOJAVE
Redward Asymmetric Blazars		
3C 279[a]	8.6	$20.58 \pm 0.79c$[d]
0954+556[a]	8.68	No Measurement
1803+784[a]	35.2	$9.36 \pm 0.87c$[e]
3C 345	6.65	$19.28 \pm 0.51c$[d]
Pearson & Readhead (1981) Sample Extreme Blazars		
0016 + 731	1.1	$8.23 \pm 0.34c$[e]
0133 + 476	20.8[b]	$16.54 \pm 0.56c$[e]
0212 + 735	7.8	$6.58 \pm 0.18c$[e]
0804 + 499	6.48	$1.02 \pm 0.26c$[e]
0836 + 710	1.1[b]	$21.10 \pm 0.77c$[d]
0850 + 581	0.4[c]	$7.56 \pm 0.38c$[e]
0859 + 470	1.0[b]	$16.1 \pm 1.3c$[d]
0945 + 408	1.12	$20.23 \pm 0.95c$[d]
1458 + 718	1.0[c]	$6.72 \pm 0.27c$[e]
1633 + 382	1.1	$29.3 \pm 1.3c$[d]
1637 + 574	1.2	$13.61 \pm 0.89c$[d]
1739 + 522	3.7[b]	No Measurement
1828 + 487	0.89	$13.06 \pm 0.14c$[d]
3CR Extreme Blazars		
3C 273	0.28	$14.85 \pm 0.17c$[d]
3C 309.1	1.0[c]	$6.72 \pm 0.27c$[e]
3C 380	0.89	$13.06 \pm 0.14c$[d]
3C 418	⋯	$6.7 \pm 1.4c$[e]
3C 454.3	3.1	$13.79 \pm 0.49c$[e]
Additional 3C Extreme Blazars		
3C 120	2.3[f]	$8.70 \pm 0.13c$[g]
3C 395	⋯	$8.81 \pm 0.24c$[e]
3C 446	8.8	$17.7 \pm 3.1c$[e]

Notes.
[a] Bright gamma-ray blazar (Ghisellini et al. 2010).
[b] Impey & Tapia (1990).
[c] Impey et al. (1991).
[d] Lister et al. (2013).
[e] Lister et al. (2016).
[f] http://www.bu.edu/blazars.
[g] Jorstad et al. (2007).

A positive value of A means that there is excess flux in the red broad wing of the BEL. For 3C 279 and 0954+556, the values were 0.64 and 1.25, respectively (Wills et al. 1995). This is extreme compared to the average of the sample of 95 quasar C IV BELs in Punsly (2010), $A = 0.039 \pm 0.219$.

In this section we begin the analysis by providing formal fits to the BELs of the most RA blazars. Our fits are decompositions based on the analysis of Brotherton et al. (1994):

1. The narrow-line (NL) region is a distant distribution of gas with emission lines characterized by an FWHM of $\leqslant 2000\,\mathrm{km\,s^{-1}}$. Radio galaxies are known to often possess very strong NL regions with an FWHM between 1500 and $2000\,\mathrm{km\,s^{-1}}$, even if there is no evidence of a photoionizing source (Best et al. 1999; Balmaverde & Capetti 2014). Theoretically, relativistic jets are expected to energize gas, thereby inducing NL emission (Bicknell et al. 1998). This is verified empirically. The correlation of $\overline{Q}$ with NL luminosity is stronger than the correlation of $L_{\rm bol}$ with the NL luminosity in radio-loud quasars (Punsly & Zhang 2011). Thus, strong NLs with FWHM $\sim$ 1500–$2000\,\mathrm{km\,s^{-1}}$ are expected in our fits to blazar spectra.
2. The broad component (BC) is produced by gas that is virialized within the gravitational potential of the central supermassive black hole. The definition of this region is sometimes conflated with the notion of the intermediate broad-line region (BLR; Brotherton et al. 1994). The BC component of the emission lines is characterized by an FWHM of $\gtrsim 2500\,\mathrm{km\,s^{-1}}$. The interpretation of lines with an FWHM of $\sim 2000\,\mathrm{km\,s^{-1}}$ as a BC or an NL is not obvious in general. Line width is strongly affected by viewing angle, in ways that are likely different from line to line (e.g., Hβ and C IV). In the case of blazars, the low value of the viewing angle makes narrow widths of the low-ionization lines more likely than in a general sample of quasars (see also Section 2.1).
3. The very broad component (VBC) is produced by gas that is virialized within the gravitational potential of the central supermassive black hole. The larger FWHM than the BC, by definition, indicates that its source lies deeper within the gravitational potential than the BC, i.e., closer to the central supermassive black hole. This second broad-line component is often required in fits to BELs. The combination of the BC and VBC composes the "full BC" component.

The background Fe II emission was subtracted using a template computed by Bruhweiler & Verner (2008). Line luminosity will be computed using the following cosmological parameters: $H_0 = 69.6\,\mathrm{km\,s^{-1}\,Mpc^{-1}}$, $\Omega_\Lambda = 0.714$, and $\Omega_m = 0.286$. The Mg II BC component fit is sensitive to the fact that Mg II is a doublet at vacuum wavelengths of $\lambda = 2976.35$ Å and $\lambda = 2803.53$ Å. The intensity ratio depends on the properties of the gas in the BLR. In Marziani et al. (2013), a ratio of the intensity of the short-wavelength line to the intensity of the long-wavelength line of 1.25 was estimated for quasars, in general. This prescription is used in our Mg II BC fits. The VBC is too broad for the doublet nature of the Mg II BEL to be significant and is ignored in our fits.

For the sake of scientific rigor, all the resultant fits need to be analyzed within the same formalism. This means that previously analyzed results will be refit. We choose the formalism of Marziani et al. (1996) in order to decompose the lines as above. The first step is to redefine the asymmetry parameter in Equation (1) as the asymmetry index, AI. First, express all wavelengths in terms of velocity relative to the laboratory of wavelength of the emission line, λ_o, i.e., $v = c(\lambda - \lambda_o)\ /\lambda_o$. The first velocity is the peak of the emission, $v_{\rm peak}$. Then, we require the red and blue velocities at 1/4 maximum and 3/4 maximum, $v_{\rm R}(1/4)$, $v_{\rm B}(1/4)$, $v_{\rm R}(3/4)$, and $v_{\rm B}(3/4)$, respectively. The line asymmetry is described by

$$\mathrm{AI} \equiv \frac{v_{\rm R}(1/4) + v_{\rm B}(1/4) - 2v_{\rm peak}}{v_{\rm R}(1/4) - v_{\rm B}(1/4)}, \tag{2}$$

$$\mathrm{C}(1/4) \equiv \frac{v_{\rm R}(1/4) + v_{\rm B}(1/4)}{2}. \tag{3}$$

We rely primarily on these empirical measures, as they are more robust than parameters that are dependent on the line-fitting method.

2.1. The Narrow-line/Broad-component Distinction

An important issue is to properly identify components that ostensibly appear to be NLs, FWHM $\sim$ 1500–2000 km s^{-1}, for these blazars. There are two competing circumstances that need to be differentiated. The ambiguity is most apparent for the low-ionization species, Mg II and Hβ, that are generally believed to originate in a planar distribution of gas in near-Keplerian motion (Wills & Browne 1986). Thus, the polar line of sight associated with a blazar will significantly reduce the FWHM that is associated with the virialized motion. Consequently, a planar virialized component can appear to have an FWHM $<$ 2000 km s^{-1} for a blazar when it would appear as an unambiguous BC for a more oblique quasar line of sight. The other complicating factor is that NLs can actually often be quite wide in radio sources (even NL radio galaxies), with FWHM $\sim$ 1500–2000 km s^{-1} being common (McCarhty 1993; Best et al. 1999). Hence, we need to be careful with our identifications of the BC. We use the following guidelines:

1. Hβ: We use an inflection point (an abrupt change in line shape or a narrow kink) between the NL and the BC to define our decomposition.
2. Mg II: The NL is very weak in general, and there is no evidence of strong NLs in radio sources (Best et al. 1999). Thus, we identify a component with FWHM $\sim$ 1500–2000 km s^{-1} as a BC.
3. Lyα: The Lyα NL can be strong in radio sources (McCarhty 1993). There is one incidence of a fitted component with FWHM $\sim$ 1500–2000 km s^{-1} (see Table 2 for 0954+556). However, there is a clear inflection point that allows us to separate a much narrower NL (FWHM $<$ 1000 km s^{-1}) from the BC.
4. C IV: The C IV NL can also be strong in radio sources (McCarhty 1993). There is one incidence of a fitted component with FWHM $\sim$ 1500–2000 km s^{-1} (see Table 2 for 0954+556). We separate an NL component by identifying a central spike (see Figure 3) with the FHWM of the Lyα NL mentioned above.

2.2. The Broad Emission Lines of 3C 279

The Mg II and C IV BELs were previously analyzed, but they are reanalyzed here in order to get a uniform data reduction of all the lines in all of our blazars (Punsly 2012; Wills et al. 1995; Netzer et al. 1995). Table 2 summarizes the results of the line fits. The first two columns are the date and the line that was observed. The third column gives the redward shift in velocity space of the VBC in the fit, followed by the FWHM and luminosity of the VBC. The next two columns are the FWHM and luminosity of the narrower BC. Columns (8) and (9) denote the FWHM and luminosity of the composite broad line, respectively. These are used in the estimators of the central black hole mass and the bolometric luminosity. The last two columns are the measures of line asymmetry that were introduced in Equations (2) and (3).

2.2.1. Redward Asymmetry and the Ionization State

The Mg II line is a low-ionization ($\approx$15 eV) emission line, and C IV is a high-ionization ($\approx$54 eV) emission line, and in principle the lines might originate in different regions of the BLR. Fortunately, both the high- and low-ionization lines of 3C 279 were observed simultaneously in 1992 April. The lines and their fits are compared in Figure 2. The high-ionization VBC is shifted more toward the red than the low-ionization VBC as shown in Column (3) of Table 2. In general, all of the 3C 279 low-ionization VBCs in Table 2, Mg II Hβ and Lyα, are shifted less than half as much as the high-ionization VBC of C IV.

2.2.2. Estimating the Bolometric Luminosity of the Accretion Flow

For the blazars that are under consideration in Table 1, the spectrum in the optical and UV bands is often dominated by the synchrotron emission from the radio jet. Thus, the continuum cannot be used to estimate the bolometric luminosity of the accretion flow, $L_{\rm bol}$. In this paper, the notion of bolometric luminosity does not include reprocessed radiation in the infrared from distant molecular clouds. This would be double-counting the thermal accretion emission that is reprocessed at midlatitudes (Davis & Laor 2011). Another method of estimating $L_{\rm bol}$ is to use the luminosity of the BELs (Wang et al. 2004). This method is more indirect. However, it is not affected by line-of-sight effects due to Doppler enhancement of jet radiation that contaminates the accretion flow continuum. Thus, we establish bolometric corrections for the BELs based on the composite quasar spectra in Laor et al. (1997) and Zheng et al. (1997) and the line strength ratios from these HST composites (Telfer et al. 2002). From the luminosity of the UV lines, we obtain bolometric corrections based on L (Mg II) and L(C IV), respectively:

$$L_{\rm bol} \approx 251 L(Mg\ {\rm II}), \quad L_{\rm bol} \approx 107 L(CIV), \tag{4}$$

as in Punsly et al. (2016).[7] We use the composite ratio from Wang et al. (2004), $L(H\beta)/L({\rm Mg\ II}) = 16.35/25.62$, in combination with Equation (4) in order to obtain a third $L_{\rm bol}$ estimator,

$$L_{\rm bol} \approx 393 L(H\beta). \tag{5}$$

Since RLQs can have very strong NLs that are enhanced by the jet excitation of the NL region, it is understood that in Equations (4) and (5) the full BC luminosity, minus the NL luminosity, is to be used in the estimate of the photoionizing source, $L_{\rm bol}$. Equations (4) and (5) are used in conjunction with the full broad-line luminosity from Table 2 to estimate $L_{\rm bol}$ using various BELs in Column (2) of Table 3.

2.2.3. Estimating the Mass of the Central Supermassive Black Hole

This section is a preliminary discussion of virial mass estimates of the supermassive central black hole. It does not include the very important line-of-sight corrections that are required to reliably apply these standard formulae to blazars. This will be addressed in Section 6. The traditional estimates presented here will be large underestimates of the black hole mass.

[7] Here we have corrected the mistake in Punsly et al. (2016) on the multiplier for Mg II (it was 151, not 251 in that paper).

Table 2
RA Blazar Broad Emission-line Fits

Date	Line	VBC Peak (km s^{-1})	VBC FWHM (km s^{-1})	VBC Luminosity (ergs s^{-1})	BC FWHM (km s^{-1})	BC Luminosity (ergs s^{-1})	Full BC FWHM (km s^{-1})	Full BC Luminosity (ergs s^{-1})	AI	C(1/4) (km s^{-1})
(1)	(2)	(3)	(4)	(5)	(6)	(7)	(8)	(9)	(10)	(11)
3C 279										
4/8/1994[i,j]	Hβ	2141 ± 72	13980 ± 8058	7.64 × 10^{42}	4810[i]	2.22 × 10^{42}	9477	9.86 × 10^{42}	0.18	2099
4/9/1992[a]	Mg II	2018 ± 95	6263 ± 235	1.20 × 10^{43}	1036 ± 106	2.40 × 10^{42}	4652	1.44 × 10^{43}	0.49	1915
4/29/2009[b]	Mg II	1351 ± 154	6404 ± 2297	5.13 × 10^{42}	2742 ± 241	4.29 × 10^{42}	3739	9.42 × 10^{42}	0.24	567
4/11/2010[b]	Mg II	1555 ± 170	6599 ± 764	5.03 × 10^{42}	2500 ± 320	2.96 × 10^{42}	3819	7.99 × 10^{42}	0.29	1025
4/8/1992[c]	C IV	5252 ± 139	10517 ± 196	3.22 × 10^{43}	3860 ± 90	1.41 × 10^{43}	5419	4.62 × 10^{43}	0.49	3762
4/8/1992[c]	Lyα	2391 ± 161	10373 ± 275	8.62 × 10^{43}	2548 ± 85	7.76 × 10^{43}	3452	1.44 × 10^{44}	0.13	616
0954+556										
12/8/1983[d,i]	Hβ	2306 ± 238	9000 ± 843	3.35 × 10^{43}	3364 ± 356	4.75 × 10^{42}	9787	3.82 × 10^{43}	0.14	4173
3/24/2012[e,i]	Hβ	2281 ± 396	8040 ± 419	2.53 × 10^{43}	2061 ± 589	6.64 × 10^{42}	4515	3.19 × 10^{43}	0.09	1454
12/8/1983[d]	Mg II	2032 ± 148	5507 ± 314	1.61 × 10^{43}	1664	7.55 × 10^{42}	2856	2.37 × 10^{43}	0.28	1401
1/12/2003[e]	Mg II	1662 ± 236	8020 ± 360	1.83 × 10^{43}	1532	7.63 × 10^{42}	3250	2.59 × 10^{43}	0.30	1610
3/24/2012[e]	Mg II	1812 ± 130	7501 ± 908	2.22 × 10^{43}	1467	6.64 × 10^{42}	3028	2.89 × 10^{43}	0.41	1466
1/20/1993[c]	C IV	3790 ± 2447	8776 ± 501	7.82 × 10^{43}	1971 ± 59	3.42 × 10^{43}	2610	1.12 × 10^{44}	0.60	2964
1/20/1993[c]	Lyα	2640 ± 369	6292 ± 656	1.02 × 10^{44}	1780 ± 93	7.99 × 10^{43}	6292	1.87 × 10^{44}	0.42	1338
1/20/1993[c]	OVI	3675 ± 314	10031 ± 220	5.89 × 10^{43}	1100 ± 204	9.18 × 10^{42}	10031	5.89 × 10^{43}	0.45	3850
1803+784										
7/04/1986[d]	Hβ	4236	5415	4.18 × 10^{42}	3765	9.19 × 10^{42}	4462	1.34 × 10^{43}	0.23	2263
7/04/1986[d]	Mg II	2465	6380	1.36 × 10^{43}	1785	6.89 × 10^{42}	2950	2.05 × 10^{43}	0.47	2016
3C 345										
6/11/2012[e]	Hβ	2382 ± 205	11123 ± 412	6.83 × 10^{42}	3185 ± 125	4.79 × 10^{42}	4010	1.16 × 10^{43}	0.22	1342
5/27/2016[f]	Hβ	453 ± 108	15429 ± 1044	1.44 × 10^{43}	2620 ± 106	2.92 × 10^{42}	4508	1.73 × 10^{43}	−0.01	482
6/7/1992[c,j]	Mg II	1454 ± 577	7130 ± 524	5.43 × 10^{43}	3355 ± 1541	4.76 × 10^{43}	4382	1.02 × 10^{44}	0.13	800
8/20/1995[c]	Mg II	3038 ± 23	9405 ± 2422	2.64 × 10^{43}	3641 ± 134	4.24 × 10^{43}	4181	7.47 × 10^{43}	0.10	391
3/24/2009[b]	Mg II	1474 ± 105	4538 ± 72	6.71 × 10^{43}	2737 ± 30	2.96 × 10^{43}	4229	9.67 × 10^{43}	0.16	1017
6/11/2012[e]	Mg II	1368 ± 71	5963 ± 152	2.54 × 10^{43}	3330 ± 62	2.17 × 10^{43}	4225	4.71 × 10^{43}	0.11	610
5/30/2016[g]	Mg II	2290 ± 165	4510 ± 206	1.62 × 10^{43}	3503 ± 81	2.45 × 10^{43}	4578	4.07 × 10^{43}	0.16	833
8/29/2016[h]	Mg II	2194 ± 207	6471 ± 368	2.01 × 10^{43}	3045 ± 499	9.48 × 10^{42}	5385	2.96 × 10^{43}	0.30	1586
9/17/2017[h]	Mg II	2265 ± 397	7026 ± 858	1.57 × 10^{43}	2993 ± 290	1.00 × 10^{43}	4543	2.57 × 10^{43}	0.32	1480
6/7/1992[c,i]	C IV	2055 ± 2713	8336 ± 1401	2.50 × 10^{44}	3136 ± 86	1.40 × 10^{44}	4471	3.90 × 10^{44}	0.28	1414
8/20/1995[c]	C IV	3029 ± 1702	10079 ± 734	7.82 × 10^{43}	3365 ± 92	1.39 × 10^{44}	3727	2.18 × 10^{44}	0.07	503

Notes.
[a] Cerro Tololo Inter-American Observatory 4 m (Netzer et al. 1995; Punsly 2012).
[b] Steward Fermi Monitoring Program (Punsly 2012).
[c] HST.
[d] Hale Telescope (Lawrence et al. 1996).
[e] SDSS.
[f] Nordic Optical Telescope.
[g] Telescopio Nazionale Galileo.
[h] Copernico Telescope, 1.8 m.
[i] Noisy spectrum. The FWHM of the BC has a large uncertainty due to line shape and noise.
[j] San Pedro Martir 2.2 m (Marziani et al. 1996).

As discussed above, for the blazars that are under consideration the optical and UV synchrotron emission tends to mask the thermal emission from the accretion flow. Thus, the continuum cannot be used in a virial estimate of the central black hole mass, $M_{\rm bh}$. Fortunately, there are estimators that are based solely on BELs. The low-ionization lines are much more reliable than the high-ionization C IV line for estimating $M_{\rm bh}$ (Trakhtenbrot & Netzer 2012; Marziani et al. 2013). There is considerable scatter in the estimations in single-epoch estimates. Thus, to moderate dispersion in our results, we choose two estimators for both Mg II and Hβ from the literature and multiple epochs. The formula from Shen & Liu (2012) using the Mg II BEL is

$$\log\left(\frac{M_{bh}}{M_{\odot}}\right) = 3.979 + 0.698\log\left(\frac{L(MgII)}{10^{44}\ \mathrm{erg/s}}\right) + 1.382\log\left(\frac{\mathrm{FWHM}}{\mathrm{km\ s^{-1}}}\right). \quad (6)$$

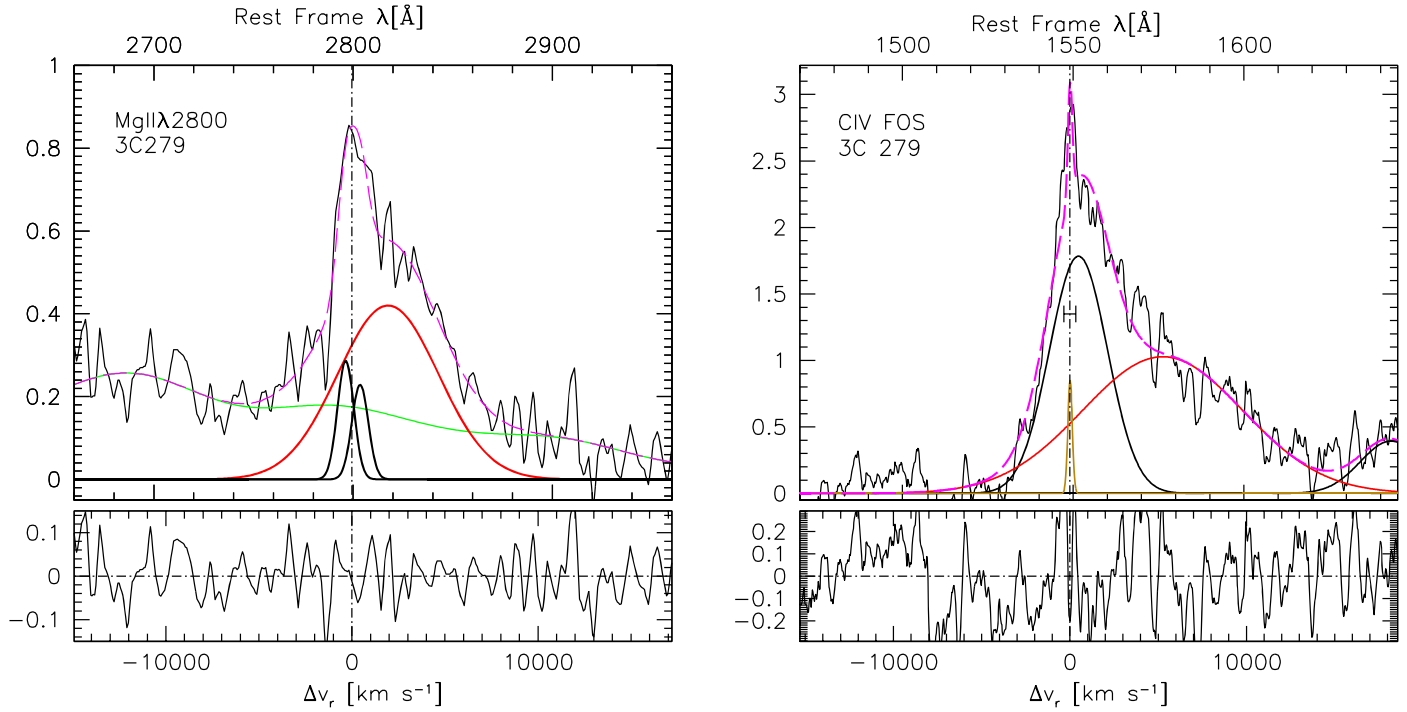

Figure 2. Simultaneous observations of 3C 279 Mg II (left) and C IV (right). Notice that the VBC is the source of the large redward asymmetry. Its center frequency is shifted toward the red. This shift is larger for the high-ionization line, C IV (see Table 2).

Alternatively, the formula of Trakhtenbrot & Netzer (2012) yields a different estimate,

$$\frac{M_{bh}}{M_{\odot}} = 6.79 \times 10^{6}\left(\frac{L(MgII)}{10^{42}\ \mathrm{erg/s}}\right)^{0.5}\left(\frac{\mathrm{FWHM}}{1000\ \mathrm{km\ s^{-1}}}\right)^{2}. \quad (7)$$

The formula from Shen & Liu (2012) using the Hβ BEL is

$$\log\left(\frac{M_{bh}}{M_{\odot}}\right) = 1.963 + 0.401\log\left(\frac{L(H\beta)}{10^{44}\ \mathrm{erg/s}}\right) + 1.959\log\left(\frac{\mathrm{FWHM}}{\mathrm{km\ s^{-1}}}\right). \quad (8)$$

The formula of Greene & Ho (2005) gives us a different estimate,

$$\log\left(\frac{M_{bh}}{M_{\odot}}\right) = 1.67 + 0.56\log\left(\frac{L(H\beta)}{10^{44}\ \mathrm{erg/s}}\right) + 2\log\left(\frac{\mathrm{FWHM}}{\mathrm{km\ s^{-1}}}\right). \quad (9)$$

Table 3 displays our estimated masses from these formulae. Table 3 justifies our motivation for using multiple lines and multiple estimators for each line; the single-epoch virial BEL estimates have a large scatter as is evident in the entries for the same object. By averaging all the Mg II line estimates together, we should obtain a more robust Mg II estimate. Similarly, we do the same to improve the Hβ line estimate of $M_{\rm bh}$. Then, we average these together in order to get our most reliable estimate.

Note that there is a large difference in the Mg II estimates and the Hβ estimate, which is disconcerting. There is a factor of ~5 difference in the estimates for 3C 279. Furthermore, the average is driven by a noisy Hβ measurement that needs to be reconfirmed with a deep spectrum during a state of low synchrotron emission. More importantly, in Section 6 we consider the effects on the $M_{\rm bh}$ estimate for the near-polar line of sight in these extreme blazars.

2.3. The Broad Emission Lines of 0954+556

Table 1 indicates that this Pearson & Readhead (1981) complete sample source is a powerful gamma-ray source that has a very high median optical polarization. There are no VLBI measurements of component motion, so it is unknown whether this is a superluminal source. There are no Mg II measurements that are contemporaneous with high-ionization line observations. The redshift of 0.899 renders the Mg II line too red to have been a natural target for HST and, unfortunately, was not observed. Furthermore, there was no simultaneous ground-based observation. However, Mg II has been very stable in the three observations spread out over 30 yr as indicated in Table 2. We chose to refit the Mg II line from 1983 in Lawrence et al. (1996) since it is such an unusual profile and requires special attention in this study. Our BC fit in Table 2 was narrower and slightly stronger than the values in Lawrence et al. (1996), 6677 km s^{-1} and 1.53×10^{42} ergs s^{-1}, respectively. Note that the three fits to the Mg II line indicate that the BC has an FWHM of ≈1600 km s^{-1}. It is formally an NL, but as we discussed in Section 2.1, this is most likely a BC that appears narrow owing to the polar, blazar line of sight. This is an important distinction since this interpretation drastically decreases the FWHM of the total BC that drives the virial mass estimates in Table 3.

The best signal-to-noise ratio (S/N) of all the observations of Mg II was the 2012 Sloan Digital Sky Survey (SDSS) observation. Thus, it is meaningful to compare it to the C IV observations. Even though the observations are not contemporaneous, as in 3C 279, the high-ionization C IV is shifted

Table 3
Derived Properties of Broad Emission-line Fits

Date (1)	Line (2)	L_{bol} (10^{45} ergs s^{-1}) (3)	M_{bh} ($10^8 M_\odot$)[a] (4)	R_{Edd} [b] (5)
		3C 279		
4/8/1994[c]	Hβ	3.88	22.4/11.6	3.09%
Average mass	Hβ	⋯	17.0	⋯
4/9/1992	Mg II	3.63	2.89/5.58	2.89%
4/29/2009	Mg II	2.37	1.59/2.91	1.89%
4/11/2010	Mg II	2.01	1.46/2.80	1.60%
Average mass	Mg II	⋯	2.87	⋯
Average mass	Hβ and Mg II	⋯	9.94	⋯
4/8/1992	C IV	4.95	⋯	3.95%
		0954+556		
12/8/1983[c]	Hβ	15.0	41.0/28.1	10.11%
3/24/2012	Hβ	12.6	8.39/5.46	8.45%
Average mass	Hβ	⋯	20.7	⋯
12/8/1983	Mg II	5.94	2.08/2.70	4.00%
1/12/2003	Mg II	6.50	2.65/3.65	4.37%
3/24/2012	Mg II	7.24	2.58/3.34	4.88%
Average mass	Mg II	⋯	2.83	⋯
Average mass	Hβ and Mg II	⋯	10.9	⋯
1/20/1993	C IV	12.0	⋯	8.09%
		1803+784		
7/04/1986	Hβ	5.27	5.79/3.02	12.43%
Average mass	Hβ	⋯	4.40	⋯
7/04/1986	Mg II	5.15	1.97/2.68	12.14%
Average mass	Mg II	⋯	2.32	⋯
Average mass	Hβ and Mg II	⋯	3.36	⋯
		3C 345		
6/11/2012	Hβ	4.56	4.43/2.25	5.66%
5/27/2016	Hβ	6.80	6.54/3.56	8.43%
Average mass	Hβ	⋯	4.20	⋯
6/7/1992	Mg II	25.6	10.4/13.6	31.7%
8/20/1995	Mg II	18.8	7.80/10.2	23.2%
3/24/2009	Mg II	24.3	9.78/12.3	30.1%
6/11/2012	Mg II	11.8	5.77/8.32	14.6%
5/30/2016	Mg II	10.2	5.83/9.08	12.7%
8/29/2016	Mg II	7.43	5.84/10.7	9.22%
9/17/2017	Mg II	6.45	4.18/7.10	8.00%
Average mass	Mg II	⋯	8.61	⋯
Average mass	Hβ and Mg II	⋯	6.40	⋯
6/7/1992	C IV	41.7	⋯	51.7%
8/20/1995	C IV	23.3	⋯	27.4%

Notes.
[a] First estimate from Shen & Liu (2012); the second estimates for Mg II and Hβ are from Trakhtenbrot & Netzer (2012) and Greene & Ho (2005), respectively. The mass estimates are not adjusted for the blazar line of sight and are likely gross underestimates (see Section 6).
[b] The Eddington rate is calculated using the mean of the "average mass" from both Hβ and Mg II. $R_{Edd} = L_{bol}/L_{Edd}$, $L_{Edd} = 1.26 \times 10^{38} M_{bh}/M_\odot$ ergs s^{-1}. These are likely gross overestimates owing to the fact that the mass estimate did not include blazar line-of-sight corrections (see Section 6).
[c] These measurements are highly uncertain owing to noisy spectra. The "out of family" mass estimates might occur for this reason. The deductions of this analysis do not depend on these values.

much farther toward the red than all three of the Mg II fits in Table 2 and Figure 3. The estimated $M_{bh} \gtrsim 10^9 M_\odot$ in Table 3, similar to 3C 279. However, as for 3C 279, there is a noisy Hβ observation from 1983 that drives this number high. If we ignore this measurement, the average mass estimate is $M_{bh} \lesssim 5 \times 10^8 M_\odot$.

2.4. The Broad Emission Lines of 1803+784

There is only one high-S/N observation of 1803+784, a very deep Hale telescope observation when the blazar was in a low optical state. Unfortunately, there was not a C IV line observation with HST. However, this is the most striking example of an RA Mg II line in the Pearson & Readhead (1981) complete sample. Thus, it is worthy of a detailed investigation.

As with the other Pearson & Readhead (1981) source, 0954+556, we refit the line (since the line shape is so unusual) instead of using the Lawrence et al. (1996) fit. The main difference in our fit is that we consider Mg II as a doublet. Our fit is in the left panel of Figure 4. The doublet nature of Mg II changes parameters of the BC. In Lawrence et al. (1996), the BC had an FWHM = 2450 km s^{-1}; in our doublet fit, the FWHM = 1795 km s^{-1}. We compare our fit to the Lawrence et al. (1996) fit in the right panel of Figure 4. There is a small difference in the blue wing of the Mg II line.

There is no C IV line for comparison of the redshifts of the VBC for the low- and high-ionization lines. However, there is an Hβ line that appears more symmetric than the Mg II line. Thus, we consider the fit in Lawrence et al. (1996) reasonable for our purposes in Tables 2 and 3. One reason that the Hβ line is so important to this analysis is that the Mg II line for 1803+784 (as well as 3C 279 and 0954+556) is very asymmetric and the notion of the FWHM is not well quantified in the context of the virial mass estimators. This creates a poorly understood uncertainty with the virial mass estimates computed from highly asymmetric profiles.

2.5. The Broad Emission Lines of 3C 345

The blazar 3C 345 appears in both the Pearson & Readhead (1981) complete sample and the 3CR complete sample. It was included in this study because it has changed from having a very mildly asymmetric Mg II BEL for two decades to having a very asymmetric Mg II BEL in the summer of 2016 (Berton et al. 2018). The emergence of the RA profile is illustrated in Figure 5. Note that the Lawrence et al. (1996) fit does not appear in Table 2 since the quality (spectral resolution and S/N) is rather poor (compared to the other spectra) and not conducive to accurate fitting. We have also obtained numerous low-S/N spectra that cannot be fit convincingly and were not included in Table 2. The HST spectra were of lower quality and required smoothing, but these are unique opportunities to simultaneously observe C IV and Mg II.

One of the topics of interest is the comparison of the redward asymmetry of high-ionization lines with that of the low-ionization lines. To this end, we processed the rather noisy HST data. For example, the 1992 Mg II data are based on only 3 minutes of observation and 4 minutes for C IV. The 1992 observation was previously discussed in Wills et al. (1995), and they found a modest asymmetry of C IV based on Equation (1), $A = 0.22$. They made no attempt to compute the asymmetry of Mg II. We proceeded to fit the HST spectra in 1992 and 1995 after some smoothing. Unlike the BELs in 3C 279 and 0954

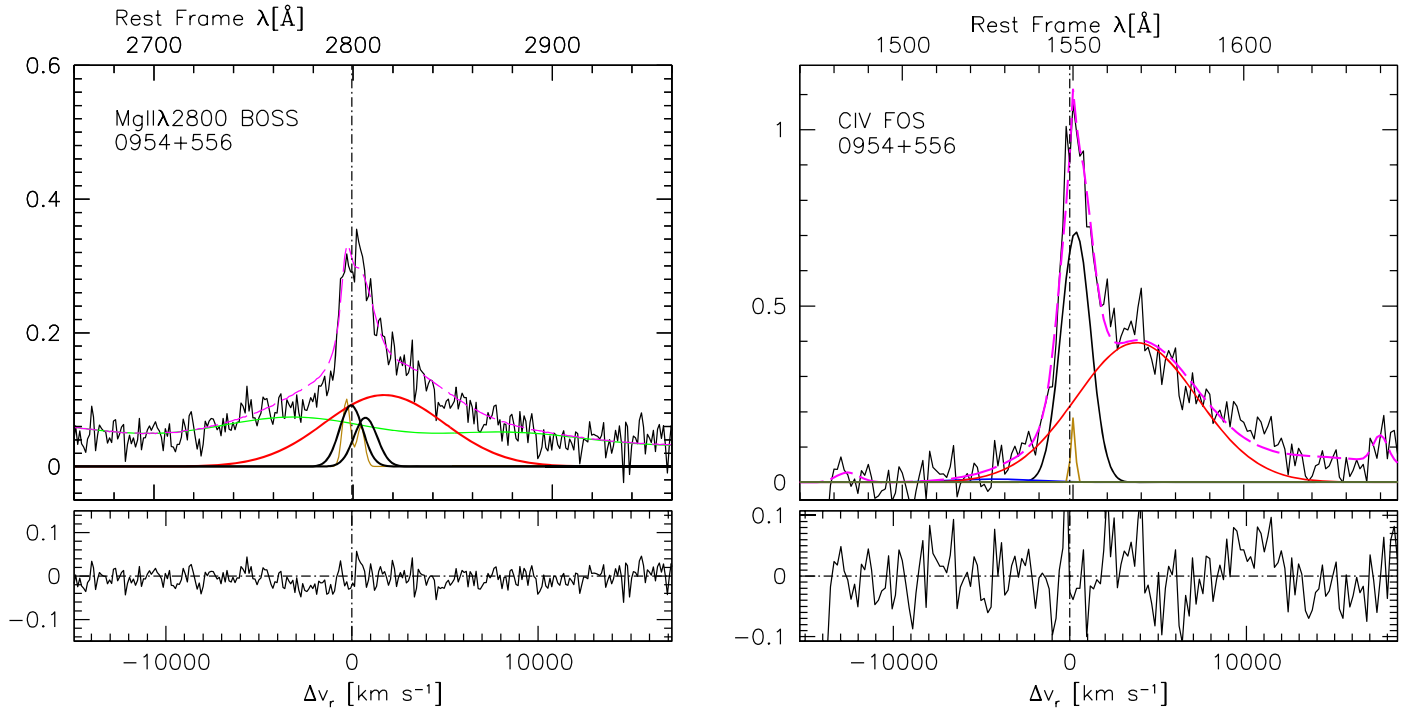

Figure 3. Nonsimultaneous observations of Mg II (left) on 2/24/2012 and C IV (right) on 1/20/1993 for the blazar 0954+556. Notice that the VBC is the source of the large redward asymmetry. Its center frequency is shifted toward the red. This shift is larger for the high-ionization line, C IV (see Table 2).

+556 (with very asymmetric BELs), Table 2 does not indicate any significant difference in the redward shift of the VBC of Mg II compared to the VBC of C IV, but the uncertainties are comparatively large. C IV does seem to have slightly larger AI and C(1/4) in Table 2 calculated from Equations (2) and (3), respectively. The observations from 1992 and 1995 represent more symmetric line shapes than we found in 2016–2017, and the Mg II line luminosity is much larger in 1992 and 1995.

3. The Jet Power

The RA quasars are distinguished by their powerful relativistic radio jets. This is clearly an important aspect of their peculiar BELs. The most basic things to look at are the line of sight and the jet power. The latter is the topic of this section.

The are two common methods of estimating the jet power, Q, of quasars. One is based on the low-frequency (151 MHz) flux from the radio lobes on 100 kpc scales (Willott et al. 1999), and the other is based on models of the broadband Doppler-boosted synchrotron and inverse Compton radiation spectra associated with the relativistic parsec-scale jet (Ghisellini et al. 2010). Each method has its own advantages. Using the parsec-scale jet, the Q estimate can be approximately contemporaneous with the observed BELs, and this is ideal for our physical understanding. However, there is a major drawback owing to small line-of-sight effects and bulk Lorentz factors of 10–50 (Lister et al. 2016). The Doppler factor, δ, is given in terms of Γ, the Lorentz factor of the outflow; β, the three-velocity of the outflow and the angle of propagation to the line of sight, θ; and $\delta = 1/[\Gamma(1 - \beta\cos\theta)]$ (Lind & Blandford 1985). The Doppler factors that are estimated are highly dependent on the line of sight, and most blazar jets are not imaged as linear structures on parsec scales but seem to typically swerve relative to any preferred linear trajectory. Thus, we know that the small angle of the line of sight to the direction of the observed structures is variable and the Doppler factor must be changing significantly for very small lines of sight and ultrarelativistic motion (Lind & Blandford 1985). Therefore, an estimate of the Doppler factor tends to vary significantly from knot to knot in the parsec-scale jet (Kellerman et al. 2004; Lister et al. 2016). The observed flux density for an unresolved ejected component depends on δ to the fourth power (Lind & Blandford 1985). Consequently, estimates of the jet power can be in error by two orders of magnitude or more (Punsly & Tingay 2005). Thus, the 151 MHz method is generally considered more reliable since it does not involve large uncertainties due to Doppler beaming (Willott et al. 1999). A disadvantage is that it involves long-term time averages, $\overline{Q}$, that do not necessarily reflect the current state of quasar activity.

Consequently, in this study we only consider the case $Q \equiv \overline{Q}$. The spectral luminosity at 151 MHz per steradian, L_{151}, provides a surrogate for the luminosity of the radio lobes in the method (Willott et al. 1999). The spectral index, α, of a power law that approximates the radio lobe spectrum is defined in terms of the spectral luminosity by $L_\nu \sim \nu^{-\alpha}$. The estimate assumes a low-frequency cutoff at 10 MHz to the spectrum of the radio lobes, that the jet axis is 60° to the line of sight, and that there is no protonic contribution and 100% filling factor. The plasma is near minimum energy, and a quantity, $\mathcal{F}$, is introduced to account for deviations of actual radio lobes from these assumptions, as well as energy lost expanding the lobe into the external medium, back flow from the head of the lobe, and kinetic turbulence. $\overline{Q}$ as a function of $\mathcal{F}$ and L_{151} is plotted in Figure 7 of Willott et al. (1999),

$$\overline{Q} \approx 3.8 \times 10^{45}\mathcal{F}L_{151}^{6/7}\text{ergs s}^{-1}. \quad (10)$$

The quantity $\mathcal{F}$ was estimated to be in the range of $10 < \mathcal{F} < 20$ for most FR II radio sources (Blundell &

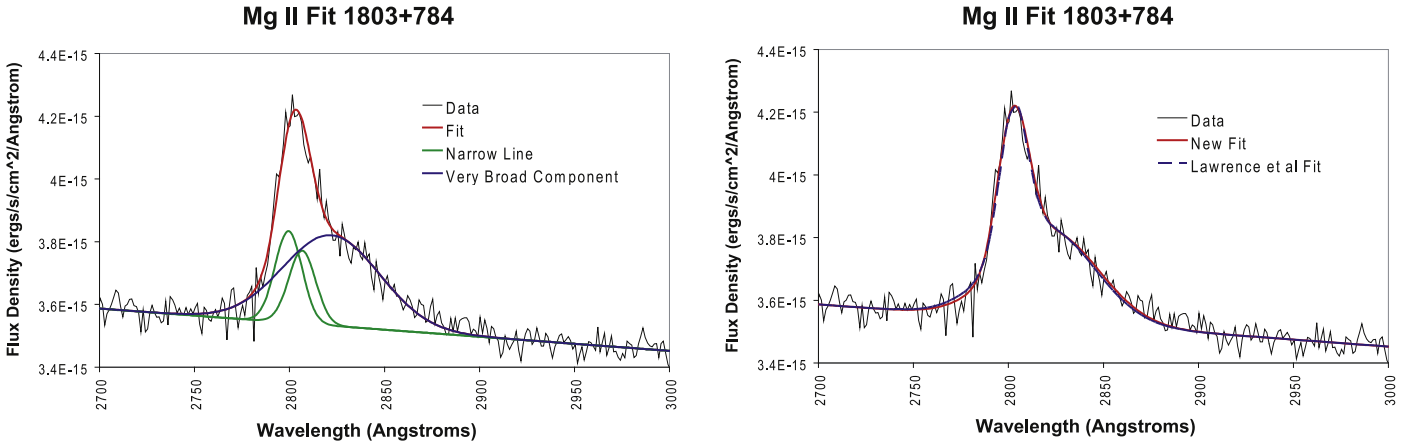

Figure 4. Fit to the Mg II line of 1803+784 from our analysis (left panel), compared to the fit of Lawrence et al. (1996) (right panel). The doublet nature of Mg II utilized in this paper made a significant difference in the width of the narrow BC and a modest difference to the fit to the blue wing of the emission line.

Rawlings 2000). We take $\mathcal{F} = 10$ for the lower bound to our estimates of $\overline{Q}$ and $\mathcal{F} = 20$ for the upper bound. This is the source of the error in the estimates in Table 4.

We note that the method is derived based on classical relaxed double radio sources. Thus, we do not consider the formula relevant for sources with a linear size of less than 20 kpc, which are constrained by the ambient pressure of the host galaxy. Furthermore, for blazars a classical relaxed double morphology is never the case. There is a very strong, dominant Doppler-boosted radio core, and the kiloparsec-scale jet tends to be Doppler boosted on the approaching side (Punsly 1995). Thus, in order to make contact with this formula, contributions from Doppler-boosted jets or radio cores are removed. This requires deep radio images with high dynamic range (the radio core is bright) as discussed in Appendix B for individual sources.

4. Distinguishing Characteristics of the RA Blazars

In this section we look for empirical characteristics of 3C 279, 0954+556, and 1803+784 that distinguish them from other similar blazars. This is crucial for understanding the physics that is responsible for the asymmetric BEL shapes. In this regard, we need to compare the blazars to complete samples of similar blazars and quantify what is meant by "similar." Based on Table 1, these are extreme objects even for blazars. Extreme in the standard notion of "blazar" means that what we see is a manifestation of an ultrarelativistic jet combined with a line of sight that is almost parallel to the direction of jet motion. Thus, we require a parent sample of objects with

1. BELs;
2. a radio jet;
3. evidence of an optically thick (due to synchrotron self-absorption, SSA, $\alpha < 0.5$) compact radio core; and
4. evidence of a line of sight that is nearly pole-on.

We choose two criteria to indicate point 4; if either is satisfied, then the object is considered to have a line of sight that is similar to 3C 279, 0954+556, and 1803+784. Either the object has high optical polarization (>3%), or the object displays superluminal motion above some threshold value. The second criterion is necessary because high-redshift, core-dominated quasars rarely show high optical polarization. Since the UV is redshifted into the optical band, one is looking much farther down the synchrotron tail than in low-redshift sources. The optically thin synchrotron tail is much steeper than the accretion disk emission spectrum per unit frequency. Thus, accretion disk emission is more pronounced in the observed optical band of high-redshift quasars. The superluminal criterion is an apparent effect due to relativistic motion. The apparent velocity, $v_{\rm app}$, can be expressed in terms of the lines of sight, θ, and the physical jet speed normalized to the speed of light, β, as

$$v_{\rm app}/c = \beta \sin\theta/(1 - \beta\cos\theta). \quad (11)$$

For polar lines of sight this can exceed 1. In order to find a $v_{\rm app}$ that represents strong blazar activity, we consult the 19 years of 15 GHz monitoring of the MOJAVE 1.5 Jy survey with the Very Long Baseline Array (Lister et al. 2016). The median fastest $v_{\rm app}$ is approximately $6c$ for these sources. Thus, we consider this a lower limit for an extreme blazar in criterion 4 above. Our sample might be slightly overinclusive; there could be a few slightly off-angle modest blazars that are mixed in with our extreme blazar sample.

In summary, our complete extreme blazar samples are subsamples of the complete high-frequency-selected (Pearson & Readhead 1981) sample of radio sources and the low-frequency-selected 3CR sample of radio sources (Spinrad et al. 1985). The conditions to define the subsamples are as follows:

1. They are Pearson & Readhead (1981) or 3CR sources, and they have
2. BELs;
3. a radio jet;
4. evidence of an optically thick compact radio core; and
5. either an optical polarization $> 3\%$ or $v_{\rm app} > 6c$.

This is the definition of the extreme blazars in Table 1. Based on Table 1, the highly RA blazars, 3C 279, 0954+556, and 1803+784, are likely much more extreme blazars than indicated by the lower cutoffs defined in criterion 5 above. However, in choosing a complete sample it is much more important to choose a sample that is overly inclusive than one that is too selective. The blazars are so extreme that we need a looser criterion for the complete samples; otherwise, there would be very few sources.

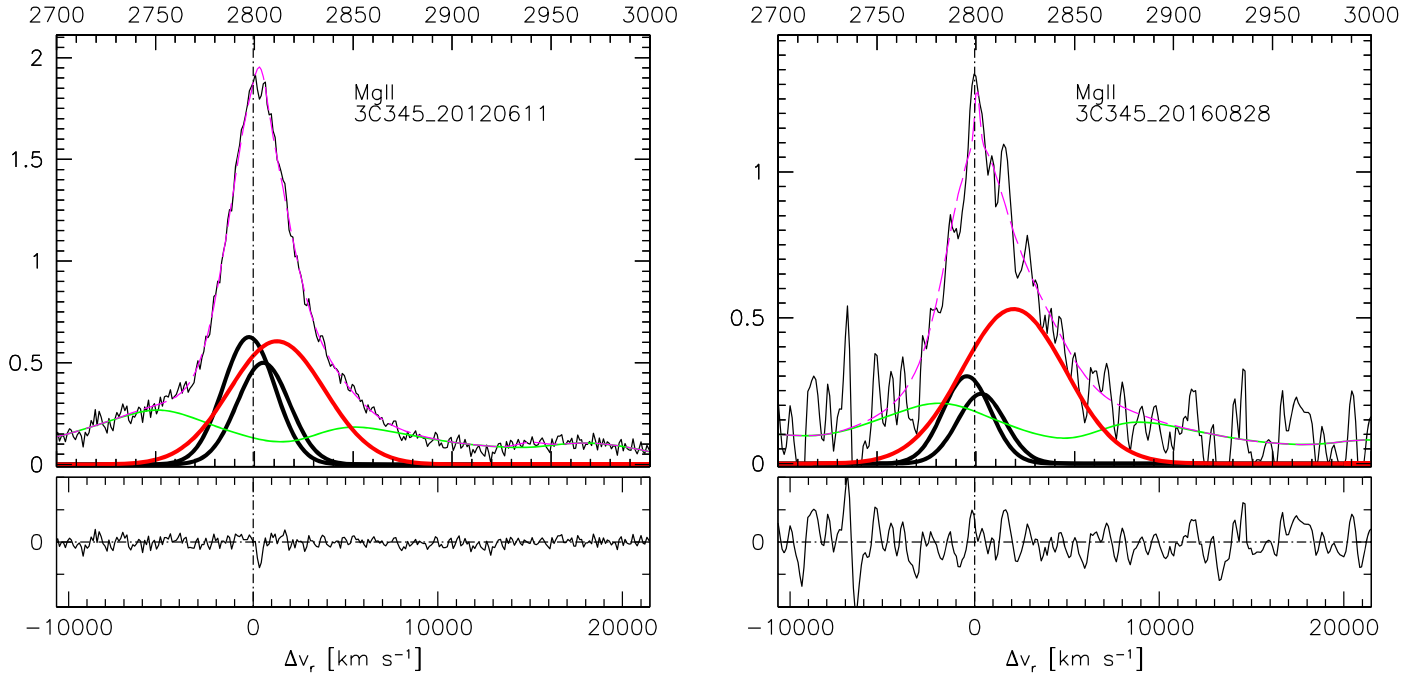

Figure 5. The Mg II BEL in 3C 345 has recently become more RA. The spectrum from 6/11/2012 (left panel) has very high S/N and shows a mildly RA profile. More recently, the BEL has become weaker. On 8/28/2016 (right panel), the BEL shows a very pronounced redward asymmetry. Notice that the VBC strength was steady during the 3 months, but the BC luminosity decreased significantly.

Table 4 provides estimates of $\overline{Q}$ that were performed using the methods that were described by means of the detailed examples in Section 3 and the Appendix. Typically, the estimates were performed with radio images of lower sensitivity and dynamic range than those in Figures B1–B3 of Appendix B. Column (2) provides the redshift of the extreme blazars. Column (3) is the detailed data extracted from the radio image that is referenced in the last column. The estimated isotropic flux (based on the methods of Section 3) is given along with the frequency of the observation. The next column is the spectral index that is used to extrapolate the extended flux to 151 MHz (observer's frame) that is discerned by the details of the image, or in some cases it also utilizes the details of images at multiple frequency. For low-quality images the default value is $\alpha = 1$. The fifth column is the extrapolated value of flux density at 151 MHz, F_{151}. The next column is $\overline{Q}$ from Equation (10).

The reason for introducing the complete samples of extreme blazars in Tables 1 and 4 is to see whether there is a distinguishing characteristic of the RA blazars that differentiates them from other similar objects—i.e., are they extreme in some other parameters. In Figure 6, we plot a suggestive scatter plane. First, we introduce the isotropic lobe luminosity (computed from Table 4) in the rest frame of the quasar, $\nu_e L_\nu(\nu_e = 151\,\mathrm{MHz})$, where the subscript "e" means emitted. From Equation (10) this translates directly to the estimate of $\overline{Q}$. Consider the bolometric correction in Equation (4) that is derived from the Mg II line strength. One can therefore define an empirical quantity that is a measure of a normalized jet power, $\nu_e L_\nu(\nu_e = 151\mathrm{MHz})/L(\mathrm{MgII})$, related to the ratio of estimators, $\overline{Q}/L_{\mathrm{bol}}$. This is the horizontal coordinate of the scatter plane in Figure 6. Similarly, based on the virial estimator in Equation (7), combined with the bolometric correction in Equation (4), we introduce the empirical vertical coordinate in Figure 6. The empirical quantity, $[L(\mathrm{MgII})]^{0.5}/\mathrm{FWHM}^2$, relates directly to estimates of the Eddington ratio, $L_{\mathrm{bol}}/L_{\mathrm{Edd}}$.

The Mg II lines used for 3C 279 and 0954+556 are from the highest-S/N spectra that were shown in Figure 1. The high 3C 345 state is from 1995, simply because the S/N was a little better than that in 1992, which lies in a similar region of the scatter plot. The low state for 3C 345 is the high-S/N spectrum with the large red asymmetry from 2016 August 28 shown in Figure 5. There is a definite pattern: the RA blazars are in the lower right corner of the scatter plot inside the dashed red rectangle. None of the other quasars in the scatter plot have a pronounced redward asymmetry in their Mg II profile. The Mg II line properties for the other extreme blazars are tabulated in Table 5. In particular, all of the quasars in Table 5 have Mg II BEL profiles with $AI \sim 0.10$ or less.

Based on Equations (7) and (10), the location in the scatter plot of the RA blazars has a natural physical interpretation: $\overline{Q}/L_{\mathrm{bol}}$ is large and $L_{\mathrm{bol}}/L_{\mathrm{Edd}}$ is small. A large value of $\nu_e L_\nu(\nu_e = 151\mathrm{MHz})/L(\mathrm{MgII})$ (an estimate for the physical quantity $\overline{Q}/L_{\mathrm{bol}}$) is not sufficient to be associated with a large redward asymmetry. The quasars 3C 446, 3C 418, and 3C 380 have very large $\nu_e L_\nu(\nu_e = 151\mathrm{MHz})/L\mathrm{MgII}$ (as large as or larger than the RA blazars). The asymmetry of the 3C 418 broad line is difficult to assess owing to some strong narrow absorption features, but it does not show any obvious signs of redward asymmetry (Smith & Spinrad 1980; Punsly & Kharb 2017). The Mg II emission line in 3C 380 is extremely well fit by a symmetric Gaussian (Lawrence et al. 1996). Figure 7 is the spectrum of 3C 446 near Mg II generously provided by Michael Brotherton. There were two observations that were combined: the McDonald Observatory 2.7 m LCS spectrum from 1991 September, and a McDonald Observatory 2.1 m ES2 spectrum from 1991 October. The spectra were consistent with each other, with similar S/N. Data were not photometric, and they were all scaled to match the flux level of

Table 4
Jet Power of Broad-line Blazars

Quasar	z	Extended Isotropic Flux Density (mJy) /Frequency (GHz)	α	Isotropic Flux Density 151 MHz (Jy)	$\overline{Q}$ (10^{45} ergs s^{-1})	Reference for Radio Image
Redward Asymmetric Blazars						
3C 279	0.536	1486/1.67	1.0	16.4	9.05 ± 3.01	Appendix B.1
0954+556	0.899	1339/0.408	1.0	3.62	7.25 ± 2.42	Appendix B.2
1803+784	0.684	67/1.55	1.0	0.69	0.98 ± 0.33	Appendix B.3
3C 345	0.593	295/1.55	1.0	3.03	2.59 ± 0.86	Appendix B.4
Pearson & Readhead (1981) Sample Extreme Blazars						
0016 + 731	1.78	7.8/1.40	1.0	0.07	1.08 ± 0.36	Kharb et al. (2010)
0133 + 476	0.86	8.7/1.40	1.0	0.08	0.25 ± 0.08	Kharb et al. (2010)
0212 + 735	2.37	1.7/1.40	1.0	0.02	0.55 ± 0.18	Kharb et al. (2010)
0804 + 499	1.43	5.3/1.55	1.0	0.05	0.49 ± 0.16	Murphy et al. (1993)
0836 + 710	2.18	730/0.408	0.96	1.90	2.73 ± 0.91	Hummel et al. (1992)
0850 + 581	1.32	244/1.40	0.8	1.45	7.49 ± 2.50	Garrington et al. (1991)
0859 + 470	1.46	222/0.408	0.9	0.54	4.00 ± 1.33	Reid et al. (1995)
0945 + 408	1.25	95/1.40	1.0	0.88	4.35 ± 1.45	Kharb et al. (2010)
1458 + 718[a]	0.91	344/4.80	0.8	5.48	10.47 ± 3.49	van Breugel et al. (1984)
1633 + 382	1.82	32/1.55	0.80	0.21	2.79 ± 0.93	Murphy et al. (1993)
1637 + 574	0.75	150/1.55	0.85	1.09	1.76 ± 0.59	Murphy et al. (1993)
1739 + 522	1.38	67/0.408	1.0	0.18	1.38 ± 0.46	Reid et al. (1995)
1828 + 487[b]	0.69	22310/0.408	0.9	54.58	42.66 ± 14.22	Reid et al. (1995)
3CR Extreme Blazars						
3C 273	0.16	2328/328	0.93	4.79	0.28 ± 0.09	Punsly & Kharb (2016)
3C 309.1[a]	0.91	344/4.8	0.8	5.48	10.47 ± 3.49	van Breugel et al. (1984)
3C 380[b]	0.69	22310/0.408	0.9	54.58	42.66 ± 14.22	Reid et al. (1995)
3C 418	2.69	2466/0.33	1.25	6.55	45.95 ± 15.32	Punsly & Kharb (2017)
3C 454.3	0.86	62/1.40	1.0	0.59	1.36 ± 0.45	Appendix B.5
Additional 3C Extreme Blazars						
3C 120	0.03	300/1.40	1.0	2.78	0.009 ± 0.003	Walker et al. (1987)
3C 395	0.64	50/1.60	1.0	0.53	0.67 ± 0.32	Saikia et al. (1990)
3C 446	1.40	340/1.60	1.0	3.60	18.63 ± 6.21	Fejes et al. (1992)

Notes.
[a] Same quasar.
[b] Same quasar.

the HST spectrum from 1991 September 11. In summary, the driver of the redward asymmetry in blazar BELs is not the jet power, alone.

The other characteristic of the zone of highly asymmetric BELs in the scatter plane of Figure 6 is the low value of $[L(\mathrm{MgII})]^{0.5}/\mathrm{FWHM}^2$ (an estimate of the physical quantity, Eddington ratio, $L_{\rm bol}/L_{\rm Edd}$). Is this alone sufficient to drive a redward asymmetry in the Mg II BEL? The scatter plot is missing sources in the lower left corner that could answer this question. This is a selection effect. Sources in the lower left corner are radio-quiet Seyfert galaxies and would not appear in the complete samples of extreme blazars. Numerous Seyfert galaxies with observed Mg II exist in this region, and none of them have pronounced redward asymmetry in their emission lines (Evans & Koratkar 2004; Kinney et al. 1991). Thus, our studies of complete samples indicate that the red dashed region is the preferred region for quasars with RA emission lines.

Even though estimates of the physical quantities have inherent uncertainty, it is useful to convert Figure 6 to physical quantities with the caveat that additional uncertainty has been introduced. The estimate for $L_{\rm bol}$ is from Equation (4). The estimate for $M_{\rm bh}$ is the average of estimates in Equations (6) and (7). The estimate for $\overline{Q}$ is from Table 4. The results are plotted in Figure 8. We note that there is one source in the preferred RA blazar sector of parameter space (the dashed red rectangle in the lower right corner) that is not an RA blazar. It is the radio source 0859 + 470. We note that the lobe flux (and therefore $\overline{Q}$) estimate is a bit uncertain based on the radio images (Murphy et al. 1993; Reid et al. 1995). There is a subarcsecond jet to the north that is likely Doppler boosted. The diffuse emission at 408 MHz is dominated by contours that are at the same level as the image noise, and the lobe flux is deemed uncertain by the observers (Reid et al. 1995). They hoped that L-band observations with the Very Large Array (VLA) would clarify the situation. The most sensitive image is from Murphy et al. (1993), but there are very strong negative contours near the source, and the diffuse features tend not to line up with those at 408 MHz. It might be that it does not belong inside the RA blazar region of the scatter plane if better L-band VLA data are obtained.

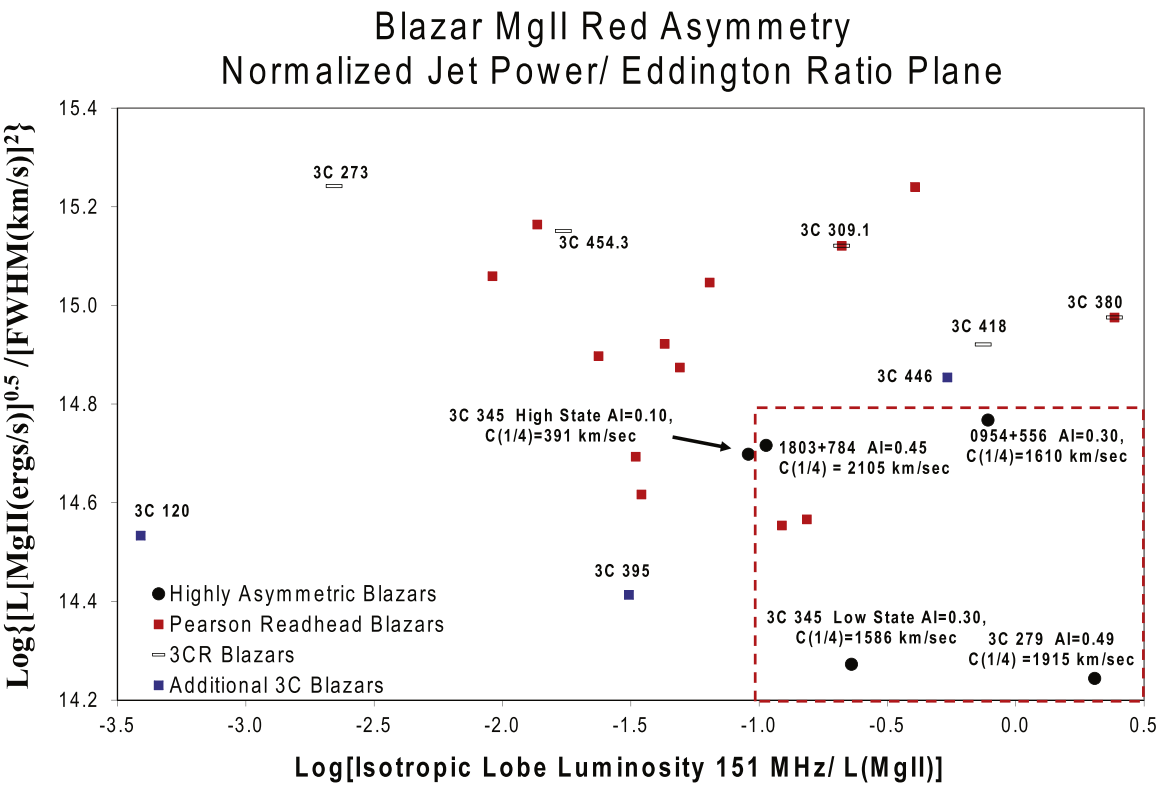

Figure 6. The scatter plot is empirical in nature. The RA blazars 3C 279, 0954+556, and 1803+784 are compared with the with two complete samples, the extreme blazars in the high-frequency-selected Pearson–Readhead sample and the low-frequency-selected 3CR sample. The horizontal axis is the large-scale isotropic low-frequency luminosity, $\nu_e L_\nu(\nu_e = 151\mathrm{MHz})$, normalized to the Mg II BEL luminosity. The vertical axis is $[L(\mathrm{MgII})]^{0.5}/\mathrm{FWHM}^2$, which is indicative of the Eddington ratio based entirely on the Mg II line.

5. The Phenomenology That Creates RA Emission Lines

In the previous section, we explored the physical aspects of the quasar that are associated with these extremely RA BELs. In this section, we explore the substructure of the BELs that creates the unusual asymmetric shape. Fortunately, Marziani et al. (2013) provide a detailed study of the nature of Mg II emission-line profiles in quasars. We can use this as a large control sample. The analysis of Marziani et al. (2013) relies on decomposing the quasar population into subsamples, Population A and Population B (Sulentic et al. 2000). Population A consists of quasars with an Hβ FWHM < 4000 km s^{-1}. Population B consists of quasars with an Hβ FWHM > 4000 km s^{-1}. RQQs can reside in either Population A or Population B, but RLQs are almost always Population B. In order to separate out extremely wide profiles, subsamples of Population B are defined. In particular, Population B1 quasars are defined by an Hβ 4000 km s^{-1} $<$ FWHM $<$ 8000 km s^{-1}. All of the RA sources in Table 1 are Population B1 quasars per Table 2.

The most obvious line characteristic to suspect as the origin of the RA Mg II BELs is the large redward peak shifts of the VBC in Table 2. These shifts are in the range of 1500–2100 km s^{-1}. This is the range of VBC shifts used in the fits of the Population B1 sources in Marziani et al. (2013), Table 2. However, by contrast, their table also indicates that these quasars have rather symmetric profiles, with the quantities from Equations (2) and (3) being

$$\mathrm{AI} = 0.07 \pm 0.03, \quad \mathrm{C}(1/4) = 230 \pm 140 \mathrm{km\,s^{-1}}. \quad (12)$$

Comparing these numbers to Table 2 indicates (surprisingly) that the 1500–2100 km s^{-1} redward shift of the VBC is not the origin of the RA profiles in these extreme blazars.

A clarification of the origin of the redward asymmetry is indicated in the scatter plot in Figure 9. The plot shows the ratio of the luminosity of the BC component to the luminosity of the VBC. Notice that the BC is actually more luminous than the VBC in Population B1 sources as indicated in Table 2 of Marziani et al. (2013) and shown pictorially in Figure 9. This is true even if we look at the subsamples from Marziani et al. (2013), B1 FR II, the FR II (steep-spectrum Fanaroff–Riley type II RLQs), or B1 CD (core-dominated RLQs). In line with this scatter plot is Figure 5. The BC is much stronger when 3C 345 has a symmetric profile than when it has an asymmetric profile. Consistent with the scatter plot in Figure 9, a strong red wing develops when the BC drops in luminosity. Figure 9 indicates that it is a weak BC relative to the VBC that produces a redward asymmetry in the Mg II BEL in these extreme blazars.

The remainder of this paper is devoted to understanding why the BC is relatively weak compared to the VBC in these RA blazars. In particular, based on the results of Section 4, we explore the creation of BELs in the context of

1. a low Eddington rate;
2. a strong jet relative to L_{bol}; and
3. a polar line of sight.

Table 5
Extreme Blazar Mg II Broad-line Properties

Quasar	Line Luminosity (ergs s^{-1}) Pearson & Readhead (1981) Sample	FWHM (km s^{-1}) Extreme	Reference Blazars
0016 + 731	7.42×10^{43}	4179	Lawrence et al. (1996)
0133 + 476	1.29×10^{43}	2946	Lawrence et al. (1996)
0212 + 735	8.13×10^{43}	2486	Lawrence et al. (1996)
0804 + 499	1.06×10^{44}	3000	Lawrence et al. (1996)
0836 + 710	2.61×10^{44}	3048	Lawrence et al. (1996)
0850 + 581	1.91×10^{44}	6214	Lawrence et al. (1996)
0859 + 470	7.33×10^{43}	4821	Lawrence et al. (1996)
0945 + 408	1.94×10^{44}	3536	Lawrence et al. (1996)
1458 + 718[a]	1.65×10^{44}	3118	Lawrence et al. (1996)
1633 + 382	1.73×10^{44}	3964	Lawrence et al. (1996)
1637 + 574	8.76×10^{43}	3536	Lawrence et al. (1996)
1739 + 522	1.38×10^{44}	3857	Lawrence et al. (1996)
1828 + 487[b]	7.48×10^{43}	3011	Lawrence et al. (1996)
	3CR	Extreme	Blazars
3C 273	2.26×10^{44}	2935	Tang et al. (2012)
3C 309.1[a]	1.65×10^{44}	3118	Lawrence et al. (1996)
3C 380[b]	7.48×10^{43}	3011	Lawrence et al. (1996)
3C 418	2.60×10^{44}	4440	Smith & Spinrad (1980)
3C 454.3	1.85×10^{44}	3100	Gupta et al. (2017); Leon-Tavares et al. (2013)
	Additional 3C	Extreme	Blazars
3C 120	2.28×10^{43}	3740	Kong et al. (2006)
3C 395	4.50×10^{43}	5090	Torrealba et al. (2012)
3C 446	1.25×10^{44}	3955	Tang et al. (2012)

Notes.
[a] Same quasar.
[b] Same quasar.

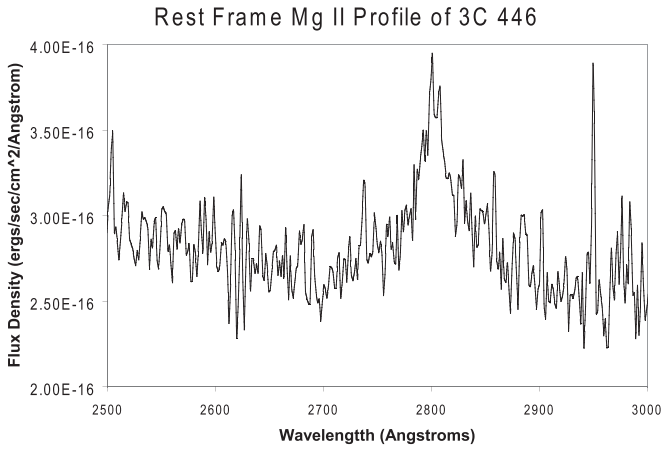

Figure 7. Symmetric Mg II BEL in the blazar 3C 446. Even though $\nu_e L_\nu(\nu_e = 151\text{MHz})/L\text{MgII}$ is large for the isotropic lobe emission, there is no dramatic redward asymmetry in Mg II.

6. The Line-of-sight-adjusted Eddington Ratio

One of the distinguishing characteristics of the BEL blazars with RA BELs is their low Eddington ratios in the scatter planes of Figures 6 and 8. Even so, these Eddington ratio estimates from Table 3 are actually grossly overestimated as a consequence of the blazar polar line of sight. The line of sight reduces the observed FWHM of the BEL and therefore reduces the estimates of $M_{\rm bh}$ in Equations (6)–(9). In this section, we recompute the Eddington ratio, $R_{\rm Edd}$, from the last column in Table 3 after correcting for a polar line of sight.

The low-ionization BEL gas is generally considered to be distributed in an equatorial disk, orthogonal to the jet axis, with a random velocity, v_r, superimposed on an equatorial velocity, v_p, that is predominantly bulk motion from Keplerian rotation (Wills & Browne 1986). For example, Jarvis & McLure (2006) use the relation

$$[\text{FWHM}]^2 \simeq 4v_p^2\left[\frac{v_r^2}{v_p^2} + \sin^2\theta\right]. \quad (13)$$

It has been estimated that $\frac{v_r^2}{v_p^2} \approx 0.024$ for the Hβ BEL (Wills & Browne 1986; Corbin 1997b). The average line of sight to the radio jet in a radio-loud quasar has been estimated as 31°, and the maximum line of sight has been estimated as ∼45° (Barthel 1989). A blazar line of sight would be $\lesssim$5° to the disk normal (Jorstad et al. 2007). According to Equation (13), if the gas were viewed within 5° of the jet axis, the FWHM would appear smaller than that of an average (steep-spectrum) radio-loud quasar by a factor $[\text{FWHM}(\theta = 5°)]^2/[\text{FWHM}(\theta = 31°)]^2$ - $= (0.024 + 0.008)/(0.023 + 0.265) = 0.11$. This can be expressed as

$$3[\text{FWHM(blazar LOS)}] \approx \text{FWHM(steep spectrum quasar LOS)}. \quad (14)$$

This was corroborated in the study of DeCarli et al. (2011), in which the host galaxy bulge luminosity estimates of $M_{\rm bh}$ were compared with virial mass estimates in order to find

$$\text{FWHM(blazar LOS)}/\text{FWHM(normal quasar LOS)} \approx 5.6/2 = 2.8, \quad (15)$$

where "normal" quasars are a mix of radio-quiet and steep-spectrum quasars. Thus, we multiply the Hβ and the Mg II FWHM in Table 2 by 2.8 and recompute Table 3 with Equations (6)–(8), and we present the results in Table 6.

Consider the estimates of $M_{\rm bh}$ for 3C 279 in Table 6. In Nilsson et al. (2009), using the empirical correlation between bulge luminosity and $M_{\rm bh}$, they found $\log\left(\frac{M_{bh}}{M_\odot}\right) = 8.9 \pm 0.5$. Using the same data, DeCarli et al. (2011) estimated $\log\left(\frac{M_{bh}}{M_\odot}\right) = 9.4$. Both estimates are consistent with our estimates in Table 6, $\log\left(\frac{M_{bh}}{M_\odot}\right) = 9.27$. The estimates in Table 6 are very crude considering the many assumptions and parameters that are not directly observed. However, the results indicate a basic conclusion, that the Eddington ratios for the RA blazars are very low for quasars, probably ∼1%–2%.

7. The Kinematics of the Redshift of the VBC

The proposed explanation in Corbin (1997a) of the very redward-shifted VBC profiles seen in some BELs was Keplerian motion and gravitational redshift of gas in a thin wedge. In order to produce line shapes, a model of the gas distribution had to be made. There is no self-consistent

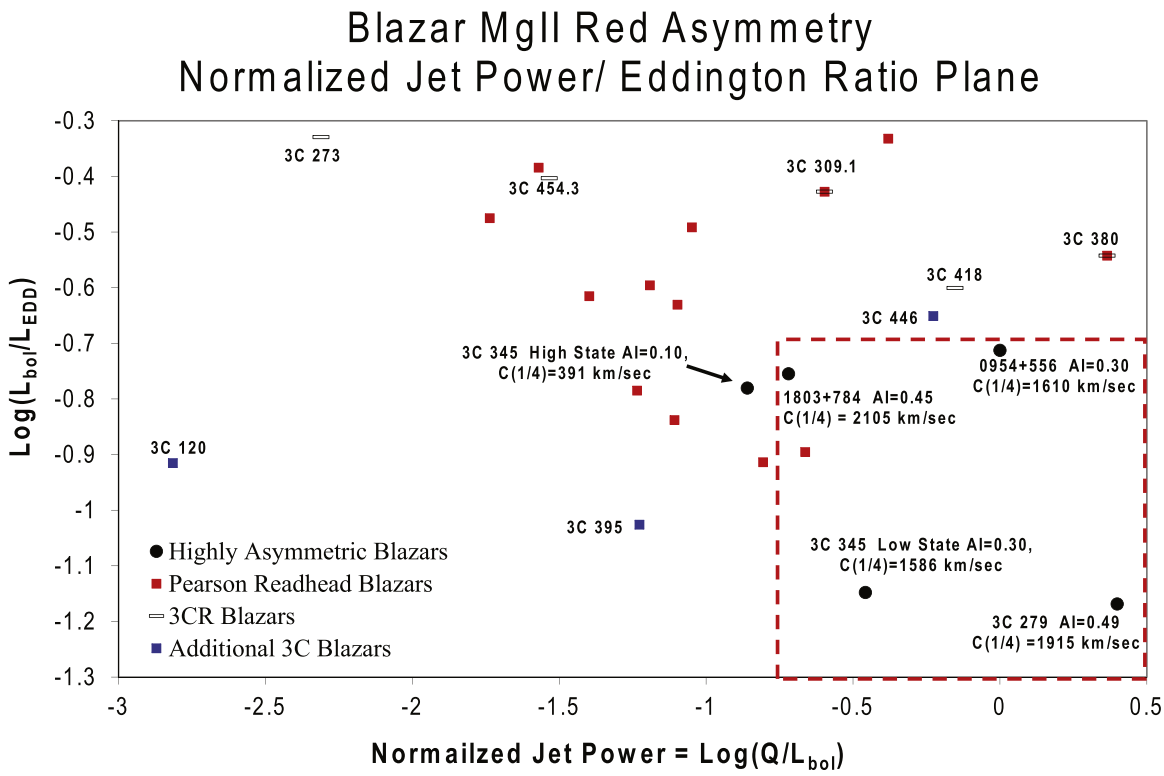

Figure 8. This scatter plot is the same as Figure 6, except that the observed quantities are converted to estimators of physical parameters by means of Equations (4), (6), (7), and (10). The RA blazars occur in the region of low Eddington rate and large jet power relative to the accretion luminosity.

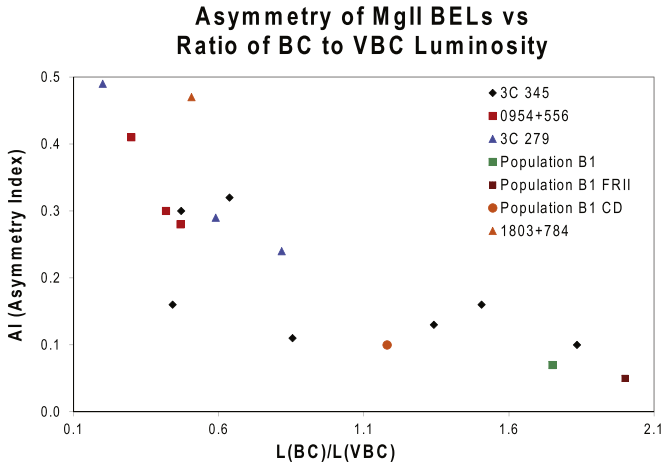

Figure 9. The scatter plot shows the dependence of C(1/4) on the ratio of the BC luminosity to the VBC luminosity. The very RA blazars have a small BC-to-VBC luminosity ratio.

modeling of the ionizing flux, gas density, and commensurate radiative transfer solution. This model is ad hoc, so it is the preference here to kinematically constrain the approximate centroid of the gas distribution composing the VBC without a specific model of the gas distribution. Namely, consider an element of ionized gas in a circular Keplerian orbit near a black hole that is emitting UV recombination emission lines at a rest-frame frequency $\nu_{\rm BEL}$. The line of sight of the observer makes an angle θ to the normal to the plane of the Keplerian orbit. The UV line emission seen at Earth is at a frequency, $\nu_{\rm earth}$, that depends on where in the orbit the element of the line-emitting gas is located. We define the frequency in the following calculation as that which is evaluated in the cosmological rest frame of the quasar, ν, and is related to that which it is observed by, $\nu = (1+z)\ \nu_{\rm earth}$. The maximum observed frequency, $\nu_{\rm max}$, is when the element is approaching Earth (maximum blueshift) at maximal velocity. Similarly, the minimum observed frequency (maximum redshift), $\nu_{\rm min}$, is when the element is an orbital location such that it is receding from Earth with maximal speed. The approximate peak of the gas distribution is defined by the frequency

$$\nu_{\rm peak} = 0.5{\rm c}(\nu_{\rm max} + \nu_{\rm min}),$$
$$\nu_{\rm earth}({\rm peak}) = [0.5{\rm c}(\nu_{\rm max} + \nu_{\rm min})]/(1+z). \quad (16)$$

In order to determine $\nu_{\rm min}$ and $\nu_{\rm max}$, we must solve for the combined frequency shift from the kinematic Doppler shift and the gravitational redshift. Since the BEL gas resides far from the black hole, spin corrections to the metric that describe the geometry external to the central black hole are negligible, justifying the use of the Schwarzschild metric. Let K^μ be the momentum four-vector of a photon emitted by the BEL gas at coordinate r. Let $U^\mu_{\rm BEL}$, U^μ_o, $U^\mu_{\rm quasar}$ be the four-velocity of an element of BEL-emitting gas in the three reference frames, the BEL gas rest frame, the local static frame, and the cosmological rest frame of quasar, respectively. All quantities in the local static frame will be designated by a subscript "o" throughout. Note that the local static frame is defined by (the following parallels problem 15.8 of Lightman et al. 1975)

$$U^\mu_{\rm quasar} = U^\mu_o \sqrt{1 - \frac{2M}{r}}. \quad (17)$$

Table 6
Estimated Line-of-sight-adjusted Properties of Broad Emission Lines

Date (1)	Line (2)	$L_{\rm bol}$ (10^{45}ergs s^{-1}) (3)	$M_{\rm bh}$ ($10^9 M_\odot$)[a] (4)	$R_{\rm Edd}$[b] (5)
3C 279				
4/8/1994[c]	Hβ	3.88	16.8/8.75	1.63%
4/9/1992	Mg II	3.63	1.20/4.38	1.52%
4/29/2009	Mg II	2.37	0.66/2.88	0.99%
4/11/2010	Mg II	2.01	0.60/2.20	0.84%
Average mass	Mg II	⋯	1.89	⋯
4/8/1992	C IV	4.95	⋯	2.08%
0954+556				
12/8/1983[c]	Hβ	15.0	30.8/22.0	3.37%
3/24/2012	Hβ	12.6	6.31/4.28	2.82%
Average mass	Hβ	⋯	5.29	⋯
12/8/1983	Mg II	5.94	0.86/2.11	1.34%
1/12/2003	Mg II	6.50	1.10/2.86	1.46%
3/24/2012	Mg II	7.24	1.07/2.62	1.63%
Average mass	Mg II	⋯	1.77	⋯
Average mass	Hβ and Mg II	⋯	3.53	⋯
1/20/1993	C IV	12.0	⋯	2.70%
1803+784				
7/04/1986	Hβ	5.27	4.37/2.39	1.93%
Average mass	Hβ	⋯	3.38	⋯
7/04/1986	Mg II	5.15	0.82/2.10	1.86%
Average mass	Mg II	⋯	1.02	⋯
Average mass	Hβ and Mg II	⋯	2.20	⋯
3C 345				
6/11/2012	Hβ	4.56	4.92/2.79	1.25%
5/27/2016	Hβ	6.80	3.33/1.77	0.84%
Average mass	Hβ	⋯	3.20	⋯
6/7/1992	Mg II	25.6	4.32/10.3	4.67%
8/20/1995	Mg II	18.8	3.24/7.97	3.44%
3/24/2009	Mg II	24.3	4.06/9.67	4.46%
6/11/2012	Mg II	11.8	2.40/6.52	2.17%
5/30/2016	Mg II	10.2	2.42/7.12	1.87%
8/29/2016	Mg II	7.43	2.42/8.40	1.37%
9/17/2017	Mg II	6.45	1.74/5.57	1.19%
Average mass	Mg II	⋯	5.44	⋯
Average mass	Hβ and Mg II	⋯	4.32	⋯
6/7/1992	C IV	41.7	⋯	7.66%
8/20/1995	C IV	23.3	⋯	4.05%

Notes.
[a] First estimate from Shen & Liu (2012); the second estimates for Mg II and Hβ are from Trakhtenbrot & Netzer (2012) and Greene & Ho (2005), respectively.
[b] The Eddington rate is calculated using the mean of the "average mass" from both Hβ and Mg II. Note that the average mass does not include Hβ for 3C 279 per table note c.
[c] These measurements are highly uncertain owing to noisy spectra. These observations are not used in average mass.

In Equation (17), we have introduced geometrized units, $M \equiv GM_{bh}/c^2$ and $c = 1$. With these definitions, one has

$$\frac{\nu_o}{\nu_{\rm BEL}} = \frac{U_o \cdot K}{U_{\rm BEL} \cdot K} = \frac{1}{\Gamma(1 - \beta \cos\phi)}. \tag{18}$$

In Equation (18), the angle ϕ is the angle between the local velocity vector and the line of sight to Earth, $\beta = v/c$ is the three-velocity of the BEL gas as measured in the static frames and $\Gamma = 1/\sqrt{1-\beta^2}$. Equation (18) is the standard kinematical Doppler shift (Lind & Blandford 1985). The transformation from the BEL rest frame to the local orthonormal static frames is equivalent to a local special relativistic boost. Similarly, one has the following transformation of the frequency from the local static frame to the quasar cosmological frame (at asymptotic infinity in the Schwarzschild metric):

$$\frac{\nu}{\nu_o} = \frac{U_{\rm quasar} \cdot K}{U_o \cdot K} = \sqrt{1 - \frac{2M}{r}}. \tag{19}$$

This constitutes the gravitational redshift. The Keplerian velocity, $c\beta_{\rm kep}$, in the static frames is (Lightman et al. 1975)

$$c\beta_{\rm kep} = \frac{d\phi_o}{dt_o} = \frac{rd\phi}{\sqrt{1 - \frac{2M}{r}}dt} = \sqrt{\frac{M}{r - 2M}}. \tag{20}$$

Note that $d\phi_o$ has units of distance since the static frames are orthonormal. Thus, combining Equations (18)–(20) at any point on the orbit, the frequency in the cosmological frame of reference of the quasar is given by

$$\frac{\nu}{\nu_{\rm BEL}} = \frac{\sqrt{1 - \frac{2M}{r}}}{\Gamma(1 - \beta_{\rm kep}\cos\phi)}. \tag{21}$$

Recall that θ is defined as the angle between the line of sight and the normal of the Keplerian plane. The maximum value of frequency in Equation (21) occurs when $\beta_{\rm kep}\cos\phi = \beta_{\rm kep}\sin\theta$, corresponding to motion toward the line of sight. The minimum value of frequency in Equation (21) occurs when $\beta_{\rm kep}\cos\phi = -\beta_{\rm kep}\sin\theta$, corresponding to motion away from the line of sight. Equation (21) therefore implies that

$$\frac{\nu_{\rm max}}{\nu_{\rm BEL}} = \frac{\sqrt{1 - \frac{2M}{r}}}{\Gamma(1 - \beta_{\rm kep}\sin\theta)}, \frac{\nu_{\rm min}}{\nu_{\rm BEL}} = \frac{\sqrt{1 - \frac{2M}{r}}}{\Gamma(1 + \beta_{\rm kep}\sin\theta)}. \tag{22}$$

From Equations (16), (22), and (23) the offset of the peak of the VBC from the systemic velocity of the quasar, $v_{\rm peak\ offset}$, does not depend on the line of sight,

$$\frac{v_{\rm peak\ offset}}{c} = \frac{\nu_{\rm peak}}{\nu_{\rm BEL}} = 1 - (\Gamma)^{-1}\sqrt{1 - \frac{2M}{r}} \approx \frac{M}{r} + \frac{1}{2}\beta_{\rm kep}^2 \approx \frac{3M}{2r}. \tag{23}$$

The first term on the right-hand side of Equation (24) is the gravitational redshift, and the second term is the transverse Doppler shift from orbital motion. The fact that the result is independent of the line of sight naturally explains the fact that the Population B1 quasars in Marziani et al. (2013) have very

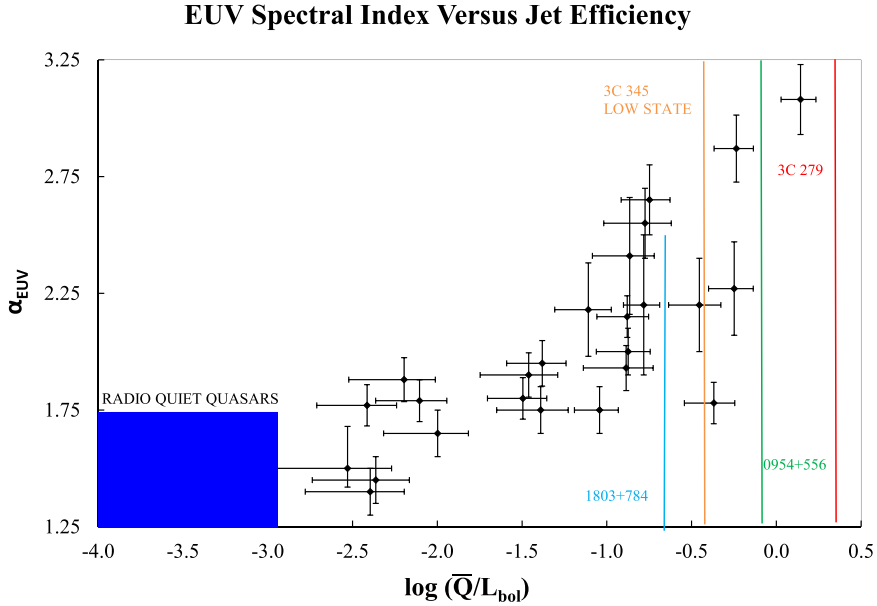

Figure 10. This scatter plot shows that the EUV deficit of RLQs is originally from Punsly & Kharb (2016). We superimpose the locations of the *x*-variable ($\overline{Q}/L_{\rm bol}$) for the RA blazars for comparison purposes. The $\overline{Q}/L_{\rm bol}$ estimates for the RA blazars are from Tables 3 and 4.

similar Mg II VBC redshifts to the nearly polar line-of-sight blazars in Table 2, $v_{\rm peak\ offset} \sim 2000\ {\rm km\ s^{-1}}$. This is compelling evidence that this is the correct explanation of the redshift as opposed to a directional outflow or inflow. If one assumes approximately Keplerian motion of the BEL gas, Equation (24) can be solved for r. A VBC peak offset of $2000\ {\rm km\ s^{-1}}$ occurs at $r = 225$ M by Equation (24). For the C IV VBC redshift of 3C 279 in Table 2, $v_{\rm peak\ offset} \sim 5000\ {\rm km\ s^{-1}}$, and by Equation (24), $r = 90$ M.[8] This leads to the natural question, how can this BEL gas reside so close to the black hole and not be too overionized to radiate efficiently?

8. The Ionization State of the VBC

The results of Sections 4, 5, and 7 indicate that the strong red wing in these extreme blazars is emitted from VBC gas deep in the gravitational potential at $r \sim$ 100–200 M. This section is an analysis of the ionization state of gas this close to the central quasar. We verify the expected trivial result that gas this close to the photoionizing source will be too ionized to radiate BELs efficiently in most quasars. We explore the conditions necessary for this region to be a bright source of BELs using Figures 6 and 8 as a guide. The low Eddington rate estimated at ∼1% in Table 6 is an obvious factor to lower the strength of the ionizing source. However, it does not explain any connection to the powerful radio jet that also appears to be relevant based on Figures 6 and 8. This section explores a possible connection to the radio jet that is based on the interaction of the radio jet launching mechanism and the innermost regions of the quasar accretion flow, a region that is the source of the EUV continuum (Zheng et al. 1997; Telfer et al. 2002). The difference imposed on the quasar spectrum associated with the jet launching mechanism was quantified as an "EUV deficit" of radio-loud quasars that increases with the strength of the jet (Punsly 2015). This is particularly relevant because these are the bulk of the photons that ionize the BEL gas. In order for gas to emit Mg II BELs, it must be singly ionized, which requires a photon of energy > 15 eV. Thus, photons with a wavelength < 825 Å are required to ionize the gas in order for Mg II BELs to occur owing to photoionization by the accretion flow radiation.

This is the EUV region of the quasar spectrum. The EUV is more important than the soft X-ray band in the photoionization of BEL clouds at a distance, R_{BC}, from the quasar, since it is the number of ionizing photons that are relevant to the degree of ionization and the number spectrum, $N_\nu \equiv L_\nu/(4\pi R_{BC}^2 ch\nu)$ (where L_ν is the spectral luminosity), is very steep in the EUV region of quasar spectra (Telfer et al. 2002). Thus, most of the ionizing photons are emitted just below 825 Å. Consider the plot in Figure 10. This plot was originally developed in Punsly (2015), and the version in Figure 10 was presented in Punsly & Kharb (2016) with some additional sources.[9] The spectral luminosity in the EUV is defined by a power law, $L_\nu \sim \nu^{-\alpha_{\rm EUV}}$. In Figure 10, $\alpha_{\rm EUV}$ is estimated in the region 1100–700 Å. We do not know the extent of the power law in general, but we assume that a continuous power-law approximation is valid shortward of 700 Å in the following. This continuum is the main source of ionizing photons. Based on Figure 10, radio-loud quasars will produce fewer ionizing photons than radio-quiet quasars with the same near-UV luminosity. The EUV deficit becomes much larger for the radio-loud quasars with very strong jets, such as 3C 279.

9. A CLOUDY Analysis of the Redward Asymmetry

In this section, we describe a single-zone CLOUDY 13 analysis of the ionization state associated with the photoionizing continuum of the reward asymmetric blazars (Ferland et al. 2013). We want to explore the roles of low Eddington rate and jet power. However, we note that radio-quiet Seyfert 1 galaxies typically have $R_{\rm Edd} = 0.01$–0.1 (Wandel et al. 1999). The low

[8] In cgs units this would be $r = 90[M_{bh}/(10^9 M_\odot)]1.45 \times 10^{14}$ cm.

[9] Note the minor change to the definition of $\overline{Q}$ in Equation (10). This induces an ∼10% change from the formulae used in Punsly (2015) and Punsly & Kharb (2016). The reasons for the minor change are described in Punsly et al. (2018), yet the results of Figure 10 are not noticeably changed by the modified formula.

Eddington states of radio-quiet Seyfert galaxies have accretion rates similar to the estimated line-of-sight corrected values of $R_{\rm Edd}$ for the RA blazars in Table 6. Yet their is no evidence of extreme RA Mg II emission lines in radio-quiet Seyfert galaxies, even in low states (Evans & Koratkar 2004; Kinney et al. 1991). However, these objects tend to have much harder EUV continua than the more luminous radio-quiet quasars (Scott et al. 2004; Stevans et al. 2014; Steffen et al. 2006). Thus, our analysis must also include spectral shape changes associated with different classes of objects, as well as the Eddington ratio and the jet power.

9.1. The Design of the CLOUDY Experiment

The CLOUDY numerical experiment will be designed to test three hypotheses.

Experiment 1: Do the SEDs associated with the low Eddington rates in Table 6 for the RA blazars enhance a highly redshifted VBC compared to the VBC induced by the SED of quasars with more typical Eddington rates, ∼10%–20% (Sun & Malkan 1989)?
Experiment 2: Does the steep EUV continuum indicated in Figure 10 for these strong jet sources enhance a highly redshifted VBC compared to the VBC excited by a broad-line radio-quiet active galactic nucleus (AGN) SED with similarly low Eddington rates, ∼1%?
Experiment 3: Is the large redward asymmetry in the BELs a manifestation of a strong VBC as opposed to a weak BC?

The second experiment shows that a low accretion rate is not a sufficient condition. It highlights the importance of the change in spectral shape in the EUV as the radio jet gets stronger. The first and third experiments will compare the line emissivity as a function of distance from the central black hole (as a function of redshift through Equation (23)) induced by two different SEDs: first, a representative RA blazar (Eddington ratio ∼ 1%) SED, and second, the average Population B1 quasar SED in Marziani et al. (2013) with a ∼12% Eddington ratio. The second experiment will compare the line emissivity as a function of distance from the central black hole (as a function of redshift) induced by the same ∼1% Eddington ratio blazar SED with that induced by a low-state Seyfert 1 galaxy SED also with ∼1% Eddington ratio.

9.2. Input SEDs

CLOUDY requires an input photoionizing spectrum in order to execute the computation of line strengths originating from different BEL densities and distances from the photoionizing source. None of our three input SEDs have complete, simultaneous observations of the ionizing continuum, EUV, soft X-ray, and hard X-ray. This is far from ideal, but it is not deleterious to our efforts since we are looking at the effect of gross changes to the ionizing spectrum. Thus, coarse approximations to the photoionizing continuum will be adequate to demonstrate large changes in the VBC luminosity. The most poorly constrained is 3C 279, for which the entire SED from the accretion flow is masked by the jet emission. However, we can indirectly estimate $L_{\rm bol}$ from the BEL line strengths through Equations (4) and (5) and Tables 3 and 6. This sets an overall normalization for the SED, and Figure 10 constrains the EUV. In order to implement these two pieces of information, we introduce a quasar SED template in Figure 11 that is based on composite spectra. The template will not be the exact SED shape at the time of observation. However, for the example of 3C 279, the normalization estimates from Equations (4) and (5) and the estimate of $\alpha_{\rm EUV}$ from Figure 10 will give us the rough estimate of the ionizing continuum that we need for the experiment.

9.2.1. The Quasar SED Template

Figure 11 is our chosen quasar SED template. The SED is associated with emission from the disk, not distant molecular clouds or the relativistic jet. It is directly related to the estimates of $L_{\rm bol}$. The SED functions to provide a crude estimate of the spectral index in regions where there are gaps in our observational measurements. The figure is based on the quasar composite spectrum in Laor et al. (1997) that was predicated primarily on the HST composite spectrum (Zheng et al. 1997). Our modification is to use newer XMM quasar X-ray spectra in the 0.5–12 keV regime and the hard X-ray data (2–100 keV) of broad-line AGNs from INTEGRAL (Piconcelli et al. 2005; Beckmann et al. 2009). The junction between the EUV and the X-ray is chosen to be ∼0.4 keV (10^{17} Hz). This region is not well defined because of the existence of a soft X-ray excess in some quasars, usually higher Eddington rate quasars (Piconcelli et al. 2005). Laor et al. (1997) have the junction (somewhat arbitrarily) at 2 keV. But the amount of soft X-ray excess in our lower Eddington rate quasars might not be very large, and we ignore it to zeroth order in our approximation of the ionizing continuum.

9.2.2. The 3C 279 SED

The SED of the accretion flow is completely obscured by the bright synchrotron power law from the relativistic jet. Our only ability to peer into the hidden disk emission is through the luminosity of the emission lines. This was the basis of the $R_{\rm Edd}$ estimates in Tables 3 and 6. The BEL luminosity for the various epochs seem to indicate $R_{\rm Edd} \sim 0.01$. We choose $R_{\rm Edd} = 0.01$, a black hole mass estimate of $M_{\rm bh} \approx 2 \times 10^9 M_\odot$ from Table 6, and the bulge luminosity estimate in DeCarli et al. (2011) in order to scale the SED template in Figure 11. Furthermore, a value of $\alpha_{\rm EUV} = 2.75$ is estimated from the normalized jet power in Figure 10. This allows us to crudely estimate the SED in Figure 12. It is loosely constrained, but it does contain the essential features of the hidden SED: an extremely low $R_{\rm Edd}$ for a quasar and an extremely steep EUV continuum for a quasar. These features are sufficient for us to perform our CLOUDY numerical experiment.

Table 7 is provided to capture the logic of how each of the SEDs was completed across the entire range of frequencies in Figures 11 and 12. The first column is the object/objects used to determined the approximate SED. The first piece of information is the normalization in the second column. Then, in the next five columns we show how all the regions of the template in Figure 11 were determined in Figure 12. The details of how the observational data were implemented in these columns are given in Sections 9.2.2–9.2.4. Figure 12 has two panels. The left panel compares the SEDs of our three types of sources. The right panel has these SEDs normalized by the Eddington luminosity of the central black hole. This gives us a scale based on M that is relevant for gauging the strength of the photoionizing source in the gravitational potential well. We proceed to describe the origins of the other two SEDs.

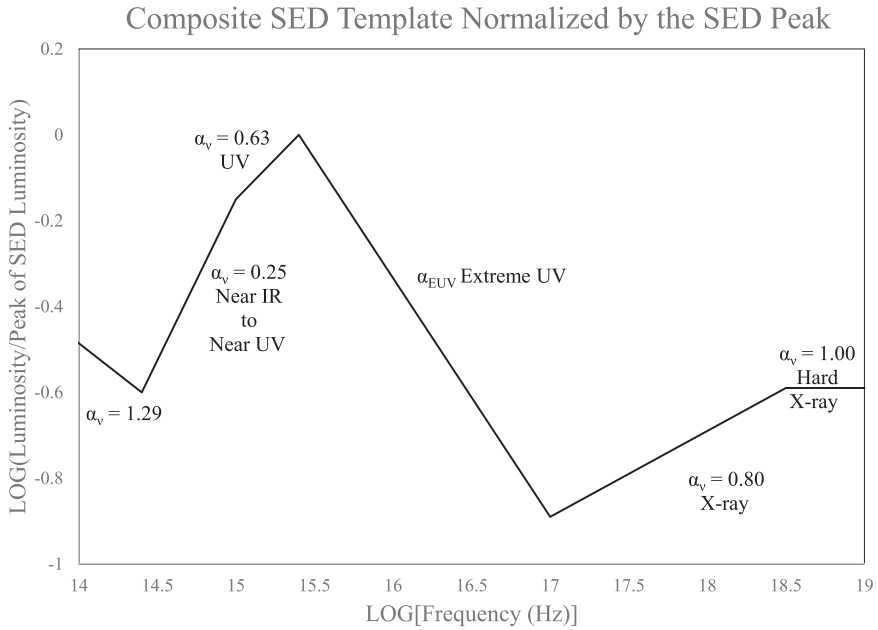

Figure 11. Quasar composite SED described in the text. We use names for the various regions (such as UV) to make contact with Table 7. The spectral indices represent power laws for the spectral luminosity $L_\nu \propto \nu^{-\alpha_\nu}$. The α_ν values from this template are used to bridge the gaps between regions of the SED that are constrained by observation. A prescription is necessary since no SED that we use has full simultaneous frequency coverage.

9.2.3. The Population B1 SED

The Population B1 quasars discussed in Section 5 were similar to the RA blazars in many respects. They are associated with large central black hole masses and small or modest $R_{\rm Edd}$. Their properties are discussed in Tables 2–4 of Marziani et al. (2013) with median values. We use these to construct a median SED in Figure 12. From Table 4 of Marziani et al. (2013), $M_{\rm bh} \approx 1.3 \times 10^9 M_\odot$. The first column of Table 3 is their estimate of $L_{\rm bol}$, which is derived from the 3000 Å luminosity ($L_{3000} \equiv \lambda L_\lambda(3000\,\text{Å})$) in their first column,

$$\log L_{\rm bol} = (9.24 \pm 0.77) + (0.81 \pm 0.02) \log L_{3000}. \quad (24)$$

We invert Equation (24) with $\log L_{\rm bol} = 46.13$ for the Population B1 quasars to find $\log L_{3000} = 45.54$. We use this point to scale the template SED in Figure 11 in order to get the SED in Figure 12. Most of the Population B1 quasars in Marziani et al. (2013) are radio-quiet, 82%. Thus, we pick $\alpha_{\rm EUV} = 1.55$ based on the radio-quiet HST EUV composite spectra with $\log L_{\rm bol} \gtrsim 46$ (Telfer et al. 2002). The resultant SED has $R_{\rm Edd} = 0.12$.

9.2.4. The SED of NGC 5548 in a Low State

We were fortunate to find a low state of NGC 5548 that was observed simultaneously in the UV and X-ray on 1990 July 4 (Clavel et al. 1992). It is not the lowest state of NGC 5448 ever observed, but it was the lowest with both UV and X-ray coverage. The simultaneity is very important since there is so much variability in this source (Clavel et al. 1992). There are tabulated continuum flux densities at 2670, 1840, and 1350 Å from IUE observations and the 2–10 keV flux from Ginga. We get a strong constraint on the EUV by extrapolating the X-ray spectrum to 0.4 keV and the far-UV continuum to just shortward of Lyα, and then connecting these with a power law. It is not exact, but it should be close. The resultant EUV spectral index is $\alpha_{\rm EUV} = 1.22$. This is a relatively hard spectrum for a broad-line AGN, but it is consistent from our expectations for a radio-quiet, low-luminosity, broad-line AGN (Telfer et al. 2002; Stevans et al. 2014; Scott et al. 2004; Steffen et al. 2006).

We choose $M_{\rm bh} = 6.7 \times 10^7 M_\odot$ based on Peterson et al. (2004), Bentz et al. (2004), and Woo et al. (2010). The input SED for NGC 5548 in Figure 12 implies that $R_{\rm Edd} \approx 0.013$. Thus, when contrasted with the input 3C 279 SED, it provides a good test of the impact of the EUV deficit of radio-loud quasars on the VBC in our CLOUDY experiment.

9.3. CLOUDY Analysis of the 3C 279 Ionizing Continuum

We ran CLOUDY for hydrogen number density, n, in units of cm^{-3} of $\log(n)$= 10, 11, 11.5, and 12. We chose five times solar metallicity as is commonly assumed in BEL studies of quasars (Korista et al. 1997). As a test of our technique, we take advantage of the quasi-simultaneous 1992 April observations of two BELs of 3C 279. We have both a low-ionization line Mg II and the C IV line (see Table 2 and Figure 2). The VBC line shifts and luminosities are fitted in Table 2. Based on our CLOUDY experiment, the simple one-zone model shows agreement of the VBC line shifts of Equation (24) and the VBC luminosity for both lines at $\log(n) = 11.5 - 12$ and an 80% covering fraction as evidenced by the top left panel of Figure 13. For direct comparison of the VBC radiative efficiency from object to object, we convert this to a rest-frame equivalent width (EW), using the local continuum from the SED in Figure 12. The CLOUDY generated EWs are plotted in the right panel of Figure 13. The dashed lines are the fitted values computed from Table 2 and the local SED continuum. We see the preference for $\log(n) = 11.5 - 12$ and an 80% covering fraction in order to be consistent with both VBCs.

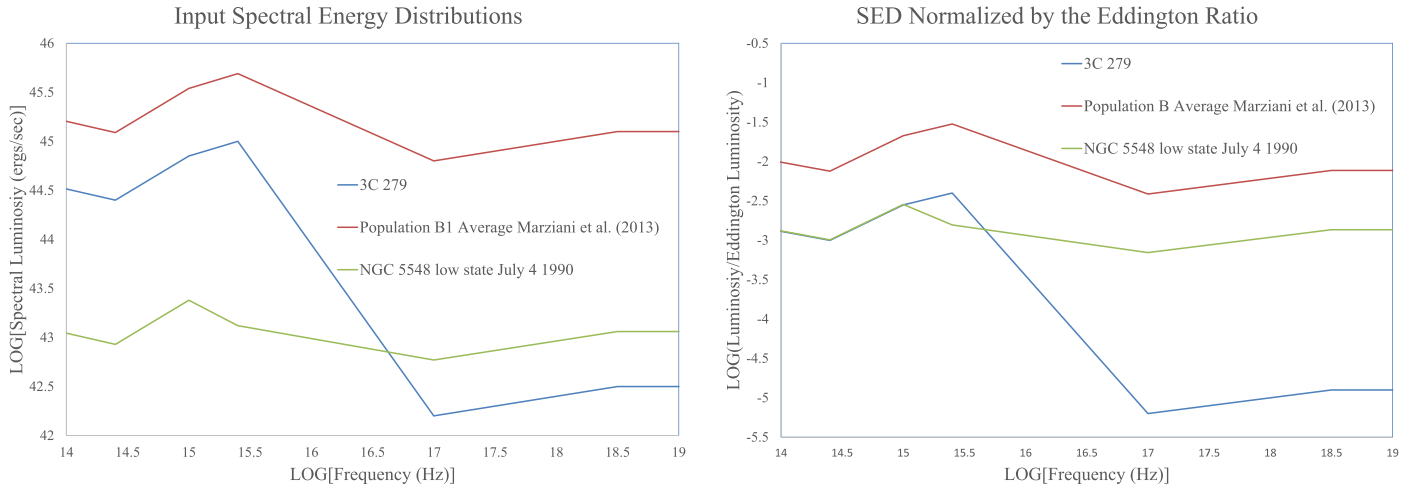

Figure 12. The three input SEDs for our CLOUDY numerical experiment as described in Section 9.2. The left panel is based on luminosity, and the right panel scales the SEDs in terms of Eddington luminosity. The red-wing asymmetric blazars are represented by the most extreme SED, 3C 279. It is very low Eddington rate and by Figure 10 is very steep in the EUV. The Population B1 SED provides a contrast between more "typical" quasars and 3C 279. The NGC 5548 low-state SED provides a contrast between low Eddington rate radio-quiet broad-line AGNs and the RA blazars.

9.4. Experiment 1: Comparing the BELs from the 3C 279 and Population B1 Ionizing Continua

Figure 13 validates that our CLOUDY analysis seems to provide reasonable results. Thus, we apply our methods to Experiment 1 from the introduction to Section 9. We compare the effect of the ionizing continuum of 3C 279 to that of quasars with conventional Eddington rates (∼10%–20%) as represented by the Population B1 SED in Figure 12. The left panel of Figure 14 shows that parameters similar to those used in Figure 13, $\log(n) \approx 12$ and an 80% covering fraction, reproduce the VBC line shift and luminosity of Mg II for both 3C 279 and the values for the Population B1 quasars (Marziani et al. 2013). The right panel of Figure 14 makes the conversion to EW by dividing the luminosity by the local continuum flux density from the SED in Figure 12. It is very reassuring that the single-zone model with a small spread in density and covering fraction is consistent with two types of quasars (Figure 14) and two ionization states of very BELs (Figure 13). Thus, we proceed to interpret the results further. The right panel clearly shows that the VBC region of the Population B1 quasars is overionized for efficient Mg II line emission as proposed in Section 8. This is not the case for 3C 279. The low Eddington rate and a steep EUV (associated with a powerful jet) in 3C 279 do not overionize the VBC near the black hole, and it radiates Mg II BELs efficiently.

9.5. Experiment 2: Comparing the BELs from the 3C 279 and a Low-luminosity Radio-quiet Seyfert Galaxy

Experiment 1 combined two control variables. It contrasted quasars with relatively weak or weak jets and a modest accretion rate with 3C 279, a quasar with a very strong jet and a low accretion rate. Thus, it is not clear whether one or both of these differences created the much stronger VBC emission in 3C 279. In formulating Experiment 2, we note that there are many low Eddington rate broad-line radio-quiet AGNs, Seyfert 1 galaxies. They do not show highly RA UV BELs (Kinney et al. 1991; Evans & Koratkar 2004; Punsly 2010). Experiment 2 explores the origin of this phenomenon with only one control variable being altered. In particular, we contrast the CLOUDY VBCs induced by the SED of 3C 279 with those induced by the low Eddington state SED of NGC 5548 in Figure 12. Figure 15 plots the Mg II VBC EW as a function of line shift from the CLOUDY experiment for the NGC 5548 low state, the Population B1 quasars, and 3C 279. The EWs are similar to the Population B1 quasars, but even smaller. Apparently, the very hard ionizing continuum compensates for the low Eddington rate and overionizes the potential VBC-emitting gas near the central black hole, with a line shift $>900\,\mathrm{km\,s^{-1}}$. In this experiment, the EUV deficit of radio-loud quasars is the sole cause of the large luminosity increase of the highly redshifted VBC of 3C 279. The experiment emphasizes the importance of the EUV deficit of radio-loud quasars in producing the RA UV BELs.

As a qualification to this experiment, it should be noted that the mean escape probability used by CLOUDY is a crude approximation to model the radiation transfer in the partially ionized zone where X-rays are absorbed. Mg II is expected to be enhanced in the partially ionized zone, so the CLOUDY predictions might be less reliable for Mg II than for a high-ionization line. The ionizing continuum of NGC 5548 has a large X-ray contribution in Figure 12. Thus, we expect that this is the least accurate of the CLOUDY experiments. However, the overionization effect is so large in Figure 15 that we do not expect this shortcoming of our calculational method to alter the conclusion of the experiment.

9.6. Experiment 3: Is the Distant BC Underionized by the 3C 279 Continuum?

A second possible explanation of the large RA seen in the UV BELs of 3C 279 is that the BC is actually weak owing to the fact that the ionizing continuum is of insufficient strength to photoionize distant gas sufficiently. We do not know exactly where the BC is located owing to the lack of a reverberation experiment. There are some estimates of the radial distance of the Mg II BLR from the quasar, R_{BLR}, based on L_{3000}. For the SED of Figure 12 for 3C 279 $L_{3000} = 7.1 \times 10^{44}$ ergs s^{-1}. The estimator based on the SDSS sample with $L_{3000} < 10^{46}$ ergs s^{-1} of Trakhtenbrot & Netzer (2012) is the most relevant

Table 7
Input SEDs for CLOUDY Experiment

SED	Normalization	Near-IR to Near-UV[a]	UV[a]	α_{EUV}[a]	X-ray[a]	Hard[a] X-ray
3C 279	R_{Edd}, M_{bh} Table 6	$\alpha_\nu = 0.25$[b]	$\alpha_\nu = 0.63$[b]	$\alpha_{EUV} = 2.75$ from Figure 10	$\alpha_\nu = 0.80$[c]	$\alpha_\nu = 1.00$[c]
Population B1	λL_λ(3000 Å)	$\alpha_\nu = 0.25$[d]	$\alpha_\nu = 0.63$[d]	$\alpha_{EUV} = 1.55$[e]	$\alpha_\nu = 0.80$[c]	$\alpha_\nu = 1.00$[c]
NGC 5548	λL_λ(1350 Å), λL_λ(2670 Å)	$\alpha_\nu = 0.25$[c]	[f]	$\alpha_{EUV} = 1.22$[c]	$\alpha_\nu = 0.80$[g]	$\alpha_\nu = 1.00$[c]

Notes.
[a] Regions of the SED are defined in Figure 11.
[b] The spectral index is from Figure 11, the SED template. Luminosity set by Eddington rate and mass from Table 6.
[c] The spectral index in the Figure 11 SED template is used to extrapolate SED from the adjacent frequency band.
[d] SED template spectral index from Figure 11. Luminosity set by median value in Marziani et al. (2013).
[e] Value from quasar composite of similar luminosity (Telfer et al. 2002).
[f] Spectrum from Clavel et al. (1992).
[g] Spectral index from Figure 11 and normalization from Clavel et al. (1992).

to 3C 279:

$$\log\left[\frac{R_{BLR}}{\text{lt}-\text{days}}\right] = (1.400 \pm 0.019) + (0.531 \pm 0.015)\log\left[\frac{L_{3000}}{10^{44}\text{ergs s}^{-1}}\right] = R_{BLR} = 71 \pm 5 \text{ lt} - \text{days}. \quad (25)$$

It is not clear how appropriate Equation (25) is to the strangely shaped BELs in Figure 1. So the results of our CLOUDY analysis that implement this value of R_{BLR} need to be viewed with caution. Using Equation (25) for our purposes is tantamount to assuming that the VBC is negligibly small in the BELs considered in the SDSS sample with $L_{3000} < 10^{46}$ ergs s^{-1} (Trakhtenbrot & Netzer 2012). For 3C 279, 71 lt-days corresponds to a Keplerian velocity of $\sim$3500 km s^{-1}.

We look at the CLOUDY results in the region around 70 lt-days from the quasar in 3C 279. These are compared to the Mg II EW for the Population B1 quasars in the same region. Figure 16 shows the results of our experiment. A major source of uncertainty in this experiment is the hydrogen number density, n. We choose $n = 10^{10}$cm^{-3}, a "standard" value for the Mg II BEL that has been used in the past (Korista et al. 1997). The figure shows that the 3C 279 SED begins to underproduce Mg II BEL emission relative to the Population B1 SED >45 lt-days from the quasar. Thus, this is a suggestive experiment that the weak ionizing continuum of 3C 279 underproduces the narrower BC components relative to more luminous radio-quiet quasars.

9.7. Summary of the CLOUDY Experiments

The simple single-zone CLOUDY experiment established that the weak ionizing continuum of the blazars with highly RA UV BELs successfully explains their existence and the properties of the VBC. In particular, we showed the following:

1. In Section 9.3 and Figure 13, it was shown that the 3C 279 SED explains the large redshifts of the VBC of both Mg II and C IV, as well as the large EWs.
2. In Section 9.4 and Figure 14, it was shown that the 3C 279 SED and the Population B1 SED explain the relative EWs of the Mg II VBC in these objects. The combination of the low R_{Edd} and the EUV deficit associated with the powerful jet in 3C 279 conspires to lower the ionizing continuum so that the nearby VBC gas does not get overionized for efficient Mg II emission. But the experiment does not elucidate the relative importance of the two causative agents.
3. In Section 9.5 and Figure 15, it was shown that the 3C 279 SED and the NGC 5548 SED in a low state explain why the VBC is weak in low-luminosity radio-quiet Seyfert 1 galaxies even though it is strong in 3C 279, which has a similarly low value of R_{Edd}. The EUV deficit is associated with the powerful jet that diminishes the ionizing continuum, allowing the nearby VBC to not be overionized in 3C 279. This experiment highlights the importance of the strong jet in the production of a strong VBC.
4. In Section 9.6 and Figure 16, it was shown not only that the 3C 279 SED creates a strong VBC that is highly redshifted but also that the low ionizing flux likely underionizes and therefore underproduces the conventional BC emission far way. The strong VBC is required for a highly RA BEL. The weak BC is a second-order effect that can accentuate the asymmetry significantly (see, e.g., Figure 5).

We note that the crude input SEDs in Figure 12 are not tightly constrained by observation, and one might question whether the inaccuracy in our SED approximations has led to a false conclusion in item 2. The driver of the redward asymmetry in the CLOUDY experiment is a depressed ionizing continuum. This cannot be observed directly in 3C 279 because of the dominant high-frequency synchrotron tail of the jet. Considering the uncertainty in the SED for 3C 279, the CLOUDY experiment is not proof that this is the cause of the highly RA BELs. We note that the input SED for 3C 279 can reproduce the velocity shift and strength of the VBC for both Mg II and C IV as indicated in Figure 13. But without directly observing the SED of the accretion flow, we cannot rule out that this is coincidental. At a minimum, the CLOUDY experiments are a consistency check of the ingredients required for highly RA UV BELs indicated in Figures 6, 8, and 10.

In Appendix A, we show that the VBC profiles can be described by the accretion disk model of Chen & Halpern

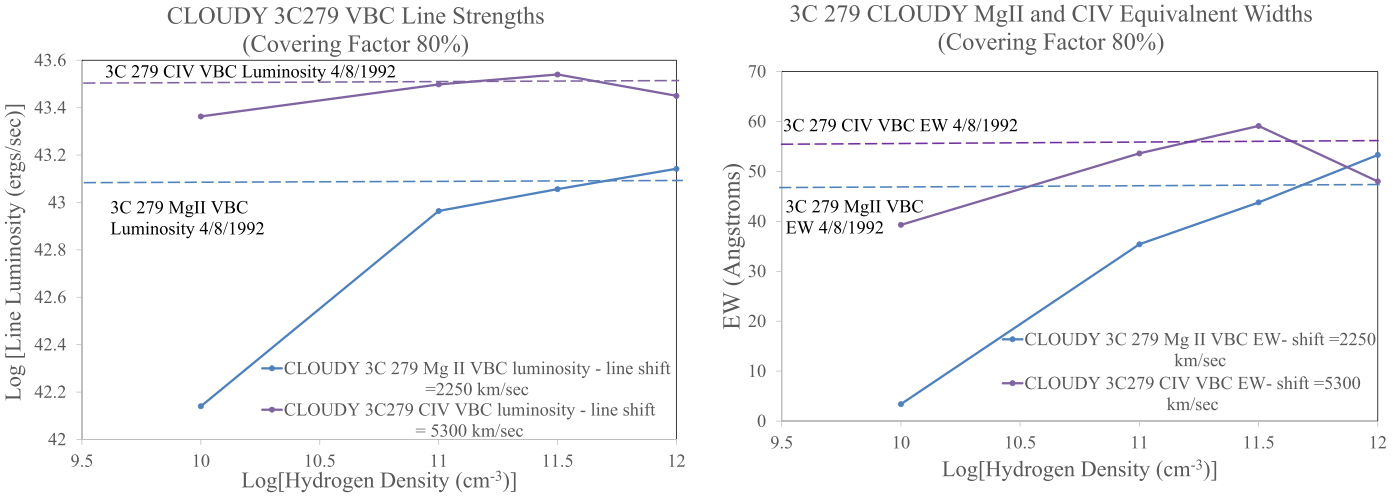

Figure 13. C IV and Mg II VBC luminosity (left) and the rest-frame EW (right) as a function of hydrogen density computed from the 3C 279 SED in Figure 12. The dashed horizontal lines are the fitted values for the VBC from 1992 April in Table 2. The emission-line (red) shifts chosen from the CLOUDY runs are the fitted line shifts in Table 2. The results show that the 3C 279 SED in Figure 12 efficiently excites a dense BEL gas, near the black hole, if $\log n = 11.5$–12 and the line strength is consistent with the observed values.

(1989), if we restrict the emitting region to being close to the central black hole as indicated in the CLOUDY experiments.

10. Comparison to Other Posited Explanations of RA UV Broad Lines

Various explanations have been offered as to the origin of highly RA BELs. We compare and contrast these with our analysis in this section.

1. Model 1: Developing an idea proposed by Popovic et al. (1995), Corbin (1997a, 1997b) suggested that the redward asymmetry arises from the VBC. It is a planar distribution of optically thin gas that is located "near" the black hole, $r \sim$100–200 M. For a nearly face-on orientation, the component of the Keplerian velocity along the line of sight is small, and the gravitational redshift is comparatively large at $r \sim$100–200 M, thereby shifting the VBC emission significantly toward the red in blazars. This is the scenario that we have developed in this paper.
2. Model 2: The BEL emission has a large component emanating from an axial flow of optically thick clouds. The unilluminated side of the clouds is dusty gas and is not a BEL emitter. The illuminated side is ionized and is a BEL emitter. Thus, we are viewing the backside of the clouds from the axial outflow on the far side of the quasar. The near-side axial outflow is undetected (Netzer et al. 1995; Wills & Brotherton 1995).
3. Model 3: There is an optically thin axial inflow in RLQs that is a powerful source of BEL emission (Netzer et al. 1995).
4. Model 4: Optically thick gas at the inner edge of the dusty torus radiates Fe II emission just redward of the BEL. These Fe II lines are the actual source of the redward emission in the BEL broad wing. Low-inclination views are shielded from the Fe II emitting gas on the near side by the dusty torus in the standard model (Antonucci 1993). For polar lines of sight all of the Fe II emitting gas is visible, hence the stronger red wings in polar (blazar) RLQs (Jackson & Browne 1991; Wills & Brotherton 1995).
5. Model 5: The BEL clouds are confined by a magnetized accretion disk wind. The blue BEL emission originates from the near-side, approaching faces of the BEL clouds. The red side of the observed BEL is light from the inner faces of the BEL clouds that is seen in reflection. The BEL emission from the inner face scatters off of electrons in the accretion disk corona back toward the observer (Emmering et al. 1992). If the scattering is primarily at small r, then the red side can be redshifted significantly as discussed in Section 7 and might cause RA BELs.

Table 8 is a direct comparison of the desired properties of a putative explanation of highly RA BELs for the various models. This is the logic table that allowed us to down-select to Model 1. Columns (2)–(6) are the properties that we motivated in this paper as being the constraints on a plausible explanation of highly RA BELs as discussed in Section 5. Column (2) is motivated by the fact that all the known sources with highly RA UV BELs are blazars (Wills & Brotherton 1995; Punsly 2010). Columns (3) and (4) are motivated by Figures 6 and 8. The requirement in Column (5) is from Marziani et al. (2013) and Table 2 as discussed in Section 5. The requirement in Column (6) is motivated by the BEL line fits in Table 2 and the line profiles in Figures 1–4. Only Model 1 complies with all these requirements. Models 2 and 3 do not require a strong jet or low $R_{\rm Edd}$. The velocity of the VBC peak shifts varies with the cosine of the line of sight to the axial flow, so it is larger ($\sim$20%) for blazars compared to Population B quasars. This violation is minor, so in of itself it is not determinant. Model 4 has no dependence on jet strength or $R_{\rm Edd}$. There is also no reason to believe that the VBC peak shift would be the same if different regions of the Fe II BLR are exposed by different lines of sight (i.e., $\sim$30° for Population B quasars vs. a polar line of sight). Model 5 would have difficulty explaining the much stronger red wings than blue wings in UV BELs in Column (6). It also has no obvious dependence on jet strength, $R_{\rm Edd}$, or the line of sight. Based on Table 8, Model 1 would appear to be the preferred explanation, but it does not categorically rule out all other explanations.

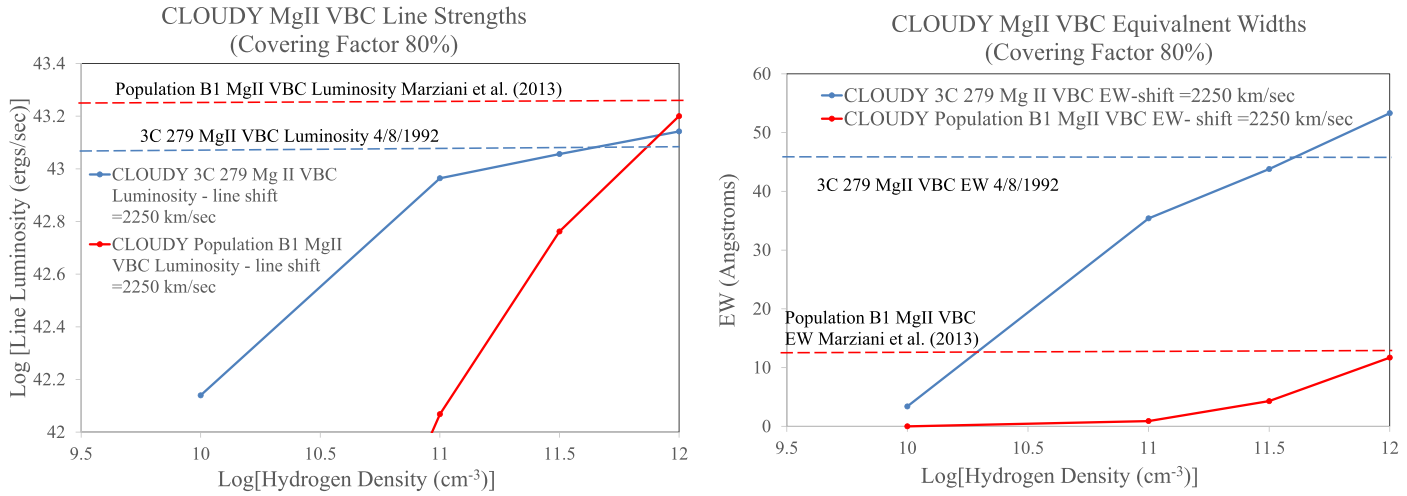

Figure 14. Comparison of the Mg II VBC luminosity (left) and the rest-frame EW (right) as a function of hydrogen density computed from the 3C 279 SED and the Population B1 SED in Figure 12. The blue dashed horizontal line is the fitted value for the VBC of 3C 279 from 1992 April in Table 2. The red dashed horizontal line is the median value from the Marziani et al. (2013) Population B1 sample. The emission-line (red) shift from Marziani et al. (2013) and for 3C 279 in 1992 are both $\gtrsim$2100 km s^{-1}. The right panel shows that the 3C 279 SED in Figure 12 efficiently excites a dense BEL gas, near the black hole, if $\log n = 11.5 - 12$, yet the Population B1 SED seems to overionize the VBC region for efficient Mg II line emission.

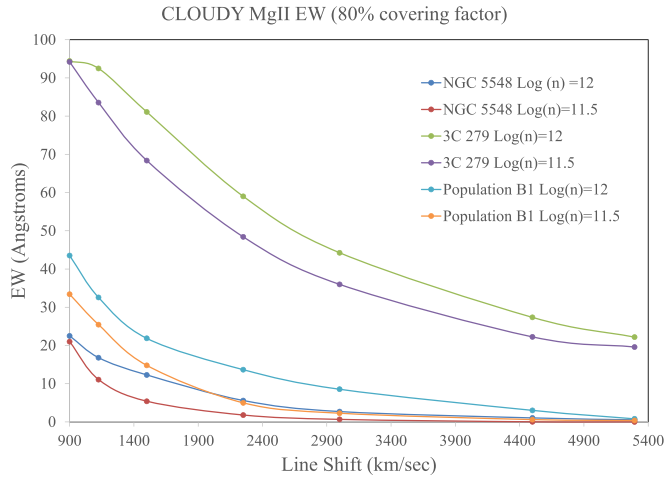

Figure 15. Comparison of the Mg II VBC rest frame EW as a function of line (red) shift computed from the 3C 279 SED, the Population B1 SED, and the low-state NGC 5548 SED in Figure 12. The figure shows that the 3C 279 SED in Figure 12 efficiently excites a dense BEL gas at large redshift, yet both the Population B1 SED and the low-state NGC 5548 SED seem to overionize the VBC region for efficient Mg II line emission to a similar degree. The NGC 5548 contrast with 3C 279, along with the input SEDs in Figure 12, shows that the steep EUV continuum associated with a powerful jet makes a profound difference on the VBC strength.

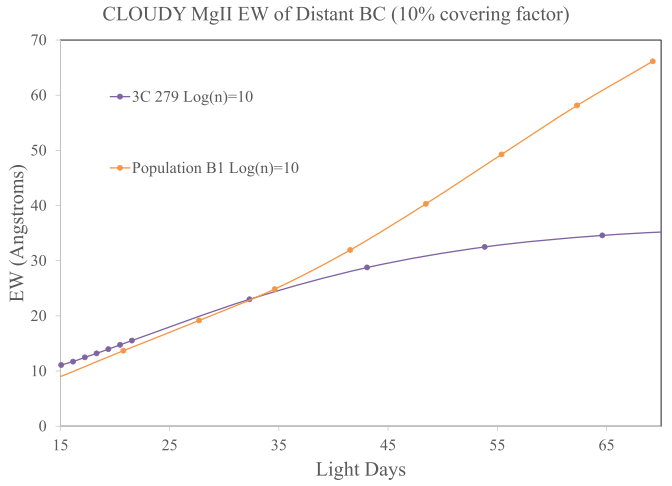

Figure 16. Comparison of the Mg II BC EW as a function of the number of light-days from the quasar computed from the 3C 279 SED and the Population B1 SED in Figure 12. From Equation (25), we estimate that the Mg II BC is ~70 lt-days from the quasar in 3C 279. The Population B1 SED induces much more efficient Mg II emission than the 3C 279 SED ~70 lt-days from the quasar. Apparently, the weak ionizing continuum of 3C 279 can underionize the distant BC gas for efficient Mg II emission.

11. Discussion and Concluding Remarks

Previous research has shown that RA UV BELs are associated with radio-loud quasars and extreme asymmetry is associated with blazars in particular (Wills & Brotherton 1995; Punsly 2010). The motivating principle of this study is that the highly RA BELs are paradoxically found in blazars (objects known for possessing the most extreme blueshifts in the universe), and this paradox is a consequence of a fundamental physical process associated with relativistic jet launching and is not a coincidence.

Our investigation began empirically. In Section 4 (Figures 6 and 8), we found that the BEL blazars with the most RA BELs were those that had both an extremely low $R_{\rm Edd}$ and a very large ratio of long-term, time-averaged jet power to accretion flow thermal luminosity, $\overline{Q}/L_{\rm bol}$. In Section 5, we summarized the elements required for the highly asymmetric lines:

1. a low Eddington rate;
2. a strong jet relative to $L_{\rm bol}$; and
3. a polar line of sight.

In Section 7, we used the enormous redshifts of the VBC in these asymmetric lines to locate the C IV VBC at ≈90 M and the Mg II VBC at ≈200 M from the central black hole in 3C 279. In Section 8, we noted that this requires a very weak photoionizing continuum; otherwise, the gas will be over-ionized near the black hole the and the VBCs will be weak. So, the investigation becomes one in which we try to understand what makes a quasar continuum a weak photoionizing source. Clearly a lower $R_{\rm Edd}$ will produce a weaker photoionizing field for a given M. We also noted a phenomenon known as the

Table 8
Compliance Matrix for the Explanations of Highly RA UV BELs

Explanation	Polar Line of Sight Required for Strong RA	Strong Jet Required for Strong RA	Low $R_{\rm Edd}$ Required for Strong RA	VBC Velocity Shift of Peak Same as Pop. B Quasars	Can Red Side of BEL Be Much More Luminous Than Blue Side of BEL?
Model 1	Yes	Yes	Yes	Yes	Yes
Model 2	Yes	No	No	No	Yes
Model 3	Yes	No	No	No	Yes
Model 4	Yes	No	No	No	Yes
Model 5	No	No	No	Yes	No

Note. Yes means compliant. No means noncompliant.

EUV deficit of radio-loud quasars (Punsly 2014, 2015). The larger $\overline{Q}/L_{\rm bol}$, the steeper (weaker) the EUV continuum as evidenced by the plot in Figure 10. 3C 279 has one of the (if not the) largest known values of $\overline{Q}/L_{\rm bol}$. We verified that it is these two elements that will produce the RA BELs (a luminous, highly redshifted VBC) with a series of CLOUDY numerical experiments in Section 9. Equivalently, we have identified two elements that create a weak photoionizing continuum and a luminous VBC at large redshift:

1. a low Eddington rate; and
2. a strong jet relative to $L_{\rm bol}$.

This is almost identical to the empirical properties of the RA blazars that are listed in the paragraph just above, but it does not include the last item: the polar line of sight. We argue that this becomes relevant because it creates a selection effect. The low-$R_{\rm Edd}$ broad-line radio-loud AGNs have enormous Doppler enhancement of the radio flux due to the polar line of sight. Thus, some rather nondescript sources appear as very bright and therefore qualify for flux-limited samples of strong radio sources. If they were viewed off-axis, they would appear as modest lobe-dominated radio sources with a weak optical core. The synchrotron spectrum would be faint, and an observer at Earth would detect the accretion flow flux in the optical band with negligible contamination from the jet emission. Based on our crude SEDs in Figures 11 and 12, we estimate a Johnson $m_v = 19.5$ ($m_v = 20.3$) for 3C 279 (0954+556) if it were viewed off-axis (i.e., $\sim 30^\circ$). Furthermore, if the BEL gas is flattened distribution of gas that rotates in the gravitational potential, for a typical quasar line of sight, from Equation (14),

$$3\,[\mathrm{FWHM(blazar\ LOS)}] \approx \mathrm{FWHM(steep\ spectrum\ quasar\ LOS)}. \quad (26)$$

Since the VBC flux is independent of the line of sight, the amplitude of the VBC Gaussian will be reduced by a factor of ≈ 3 in order to accommodate the ≈ 3 times larger FWHM. The VBC FWHM would be $\sim 15{,}000\ \mathrm{km\ s^{-1}}$. In summary, these quasars would appear with very faint (but blue) optical cores and very squat BEL profiles. These spread-out BELs would make a small contrast relative to the underlying continuum and the Fe II emission. A good example of such a wide Mg II BEL in a lobe-dominated quasar is 3C 68.1 (Smith & Spinrad 1980; Aars et al. 2005). Considering this example and noting the weak optical core for these blazars, they might be identified as radio galaxies if viewed off-axis. However, in practice, the diminished prominence of the BEL would make a VBC/BC decomposition impractical. It would be extremely challenging to get an observation good enough to reliably determine the degree of redward asymmetry, AI, and C(1/4) from Equations (2) and (3).

This discussion allows us to understand the nature of the selection effects that associate the most RA UV BELs with the polar line of sight. There are two cases:

1. There are Fanaroff–Riley II (FR II; see Fanaroff & Riley 1974 for a definition) steep-spectrum quasars with modest RA UV BELs (Barthel et al. 1990; Punsly 2010). However, the asymmetry is not as strong as in Figure 1. For these to be known quasars, $R_{\rm Edd}$ is typically at least an order of magnitude larger than that of 3C 279. Thus, the redward asymmetry is only driven by one of the two factors, the EUV deficit of radio-loud quasars.
2. The other possibility are the FR II quasars with $R_{\rm Edd} \sim 0.01$. However, as noted above, if viewed off-axis, they might be considered radio galaxies. Even if the squat broad lines were identified, it would not likely be possible to do more than a crude single Gaussian fit with no asymmetry information. We note that since the highly RA BELs are associated with quasars at the very high end of the $\overline{Q}/L_{\rm bol}$ distribution, they are rare (Punsly 2007). We searched the literary archives for $m_v \sim 20$, 4C and 6C radio sources in order to try to find an object with squat RA BELs, but we have been unsuccessful.

Appendix A
Relativistic Accretion Disk Model Fits to the Blazar C IV and Mg II VBC

The relativistic line shifts computed in Section 7 and the CLOUDY results in Section 9 indicate a mutually consistent dynamic in which the C IV (Mg II) VBC emission originates from very close to the central black hole, $r \sim 90$ M ($r \sim 225$ M). The accretion disk itself (or a portion thereof) is such a distribution of gas capable of line emission if illuminated by ionizing radiation. Thus, it is of interest to explore a parametric model of the accretion disk as the source of the VBC (Chen & Halpern 1989). It is beyond the scope of this work to justify whether the model results from a physically consistent distribution of gas, ionization state, and emissivity. The model, through its parameterization, does determine an emissivity profile that is consistent with the VBC profiles in Table 2 and Figure 2, 3, and 5.

The panels of Figure A1 show the C IV and Mg II total BEL (in black) and VBC (in red) profiles of the extreme blazars 3C 279, 0954+556, 3C 345, and 1803+784 with superimposed model profiles (in orange) of a relativistic, geometrically thin

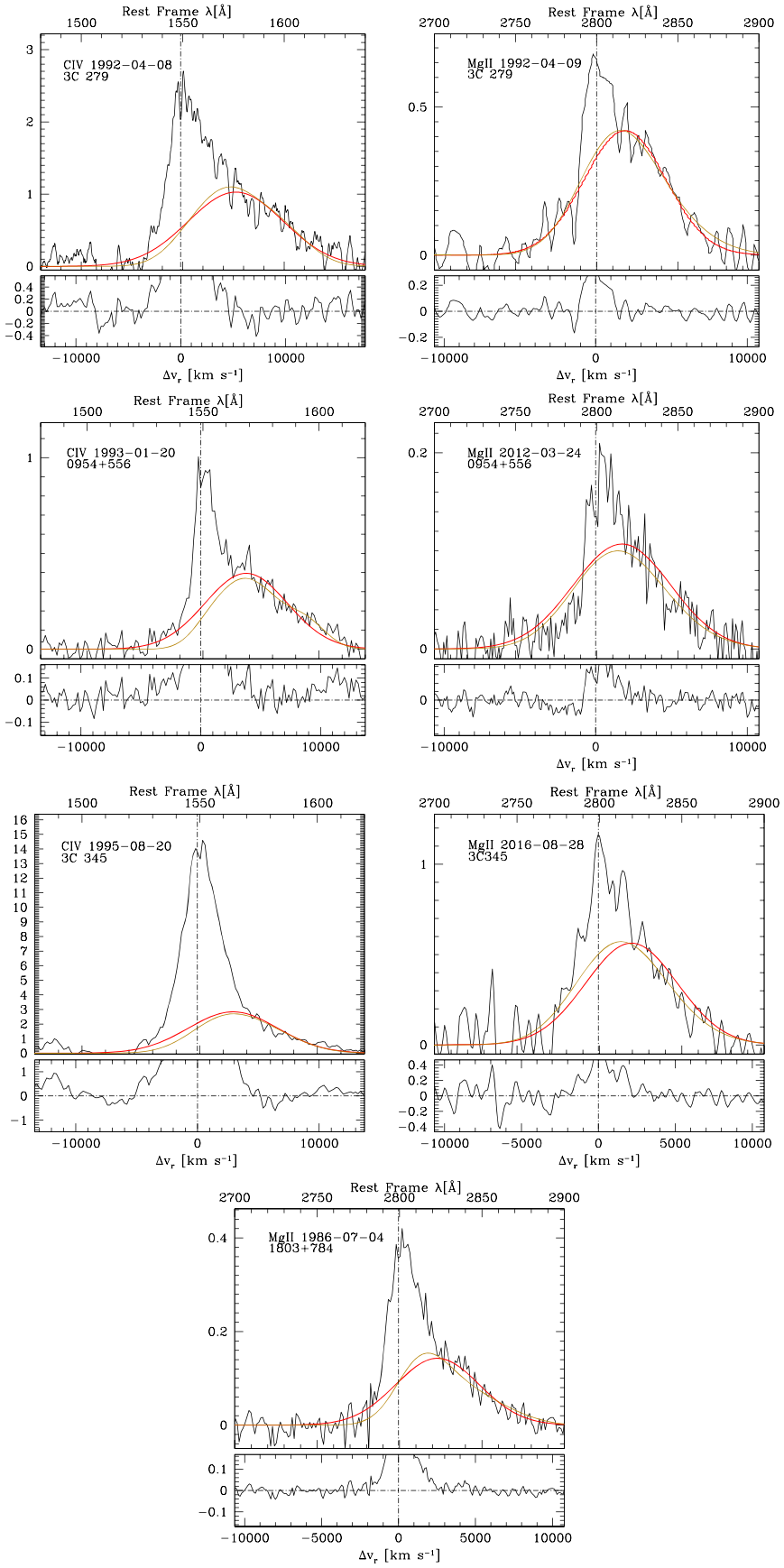

Figure A1. Relativistic accretion disk model profiles and empirical VBCs for C IV (left column) and Mg II (right). The red line traces the VBC derived from the multicomponent line fit in Table 2, and the orange profile is the accretion disk model fit whose parameters are reported in Table 9.

Table 9
Accretion Disk Parameters

Source	Line	q[a]	σ[b]	λ_0	r_{in}	r_{out}	i
3C 279	C IV	3.5	8.0E-3	1549.	60	10000	5
3C 279	Mg II	2.0	7.5E-3	2800	80	1100	4
0954+556	C IV	3.5	5.0E-3	1549	60	10000	5
0954+556	Mg II	1.5	9.0E-3	1549	100	800	5
3C 345	C IV	3.5	8.0E-3	1549	80	10000	5
3C 345	Mg II	1.3	9.0E-3	2800	80	800	2
1803+784	Mg II	2.0	5.0E-3	2800	60	700	2

Notes.
[a] Exponent of the radial emissivity law $\epsilon(r) \propto r^{-q}$.
[b] Local broadening parameter defined by Chen & Halpern (1989).

accretion disk (Chen & Halpern 1989). The model parameters are reported in Table 9, which lists them in the following order: source, line fitted, exponent of power law representing radial disk emissivity ($\epsilon \propto r^{-a}$), local broadening parameter q, reference wavelength, inner radius r_{in} of the emitting region and outer radius r_{out} of the emitting region (both in units of gravitational radii), and inclination of the accretion disk axis with respect to the line of sight.

The chosen parametric disk model profiles reproduce the empirical VBC very accurately in all instances. The models can fully account for the extended red wing typical of the extreme blazars (Figure A1) for both C IV and Mg II. From Table 9 we derive the following:

1. Orientation values are always less than or equal to 5 degrees. This result is consistent with the blazar nature of the sources, and all blazars are believed to be oriented with the jet/disk axis close to the line of sight (Urry & Padovani 1995).
2. The inner radius of the emitting portion of the disk has to be very small, less than 100 gravitational radii. The velocity field of a geometrically thin, optically thick accretion disk is expected to remain almost Keplerian down to the innermost stable orbit. From Equation (24), $r_{in} < 100$ M for the C IV VBC and $r_{in} < 225$ M for the Mg II VBC in 3C 279 and 0954+556 based on kinematic constraints. This was also corroborated by the CLOUDY results in Figure 13. The values of r_{in} from the disk models in Table 8 are consistent with these bounds.
3. To account for a large peak shift, the r_{out} should be relatively small, or the emissivity extremely steep ($a \gg 1$). The small inclination ensures that the blue Doppler-boosted peak and the red peak are blended together.
4. The q local broadening parameter is relatively large with respect to the original value derived by Chen & Halpern (1989) for Arp 102B. This ensures a smooth, almost Gaussian-like appearance for the disk model.

Appendix B
Detailed Lobe Luminosity Estimates for Individual Sources

This appendix provides new radio images and data analyses in order to supplement the jet power estimates in Section 3.

B.1. The Extended Diffuse Flux of 3C 279

Even though 3C 279 is perhaps the best-known example of the blazar phenomenon, no deep image of the extended emission has ever been published. The best image that we have is a C-band image with the early VLA (de Pater & Perley 1983). Due to the steep-spectrum nature of extended flux, C-band (~5 GHz) images tend to resolve out diffuse emission and require higher dynamic range than L-band (~1.4 GHz) images (the core being that flat spectrum contributes more to the total flux density at high frequency). Equation (10) requires deep images for the proper extraction of the isotropic diffuse extended flux. To this end, we present the first deep L-band image of 3C 279 in Figure B1. The observation was with the VLA in A-configuration on 2001 January 11. The observing frequency was 1.665 GHz, and the image was restored with a 1.5″ circular beam.

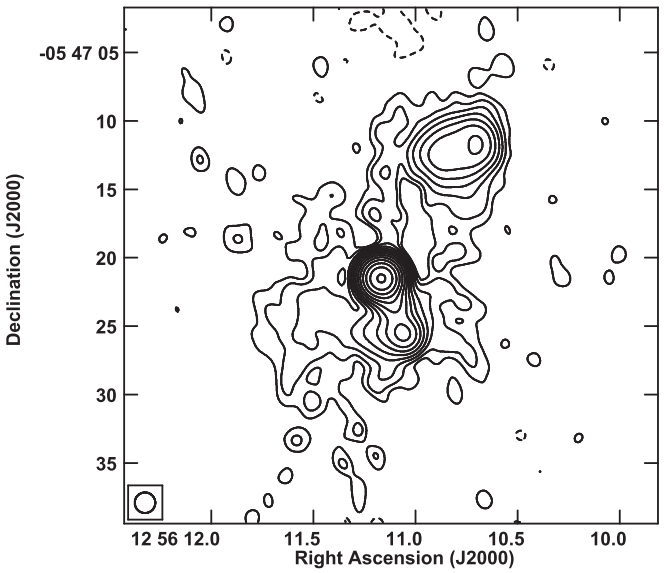

Figure B1. The 1665 MHz image of 3C 279. The radio contours are in percentage of peak surface brightness (=10.2 Jy beam^{-1}) and increase in steps of 2, with the lowest contour being ±0.02%. The jet points toward the south. Note the luminous radio lobe to the north and the diffuse halo type emission.

The image is useful for extracting the isotropic extended emission. The beamed emission originates in the core and possibly in the kiloparsec jet to the south. A conservative estimate of the isotropic diffuse flux is therefore obtained by subtracting the core plus jet flux density (11.11 Jy) from the total flux (12.60 Jy) in order to yield an extended isotropic flux density of 1.49 Jy. Figure B1 shows a large amount of diffuse structure. Thus, the A-configuration observation has undoubtedly resolved out some diffuse emission. To properly constrain the total lobe flux density would require a P-band observation with the new correlator of the Jansky VLA. An L-band B-configuration observation would also be helpful. For now, we must work with the L-band image in Figure B1 in order to extrapolate the emission to 151 MHz. Considering the large diffuse cloud of emission and the conservative estimate above, a spectral index of $\alpha = 1$ seems reasonable for the extrapolation from 1.665 GHz (Kellermann et al. 1969). This yields 16.4 Jy at 151 MHz for the isotropic emission. From Equation (10) with $10 < \mathcal{F} < 20$, this equates to an estimate of the long-term time-averaged jet power of $\overline{Q} = (9.05 \pm 3.01) \times 10^{45}$ ergs s^{-1}. Based on the deep observations of blazars in Murphy et al. (1993), 3C 279 has one of the largest $\overline{Q}$ of any known blazar.

B.2. The Extended Diffuse Flux of 0954+556

Fortunately, excellent images of this blazar exist in the literature. The 408 MHz MERLIN observation in Reid et al. (1995) is of closely matched resolution with the Murphy et al. (1993) 1.552 GHz VLA observation. This allows us to compute a spectral index of 0.95 for the extended emission. The object appears to be a triple that is viewed along the jet axis, making the object appear much more compact than it actually is. The symmetry of the object indicates that there is very little if any Doppler beaming on kiloparsec scales. Extrapolating the extended 408 MHz flux density of 1.339 Jy to 151 MHz with a spectral index of 1 yields a flux density of 3.26 Jy. From Equation (10) with $10 < \mathcal{F} < 20$, this equates to an estimate of the long-term time-averaged jet power of $\overline{Q} = (7.25 \pm 2.42) \times 10^{45}$ ergs s^{-1}. As for 3C 279, this is an extremely large time-averaged jet power for a blazar.

B.3. The Extended Diffuse Flux of 1803+784

The source 1803+784 does not have the large isotropic flux that occurs in the other three RA blazars that are discussed in this appendix. It has a very distant secondary 45″ away that has been shown to be connected to the powerful radio core (Britzen et al. 2005; Antonucci & Ulvestad 1985). There is a large halo of very diffuse radio emission that has never been detected by the VLA (Britzen et al. 2005). The distant secondary is resolved, and the measured flux density in L band depends on the beam size and u–v coverage used with the VLA. The flux density of the secondary was found in Murphy et al. (1993) in the combined A- and B-configuration observations, which were optimized for u–v coverage to be 67 mJy at 1.552 GHz. No halo emission was detected. We looked at archival P-band VLA observations in order to see evidence of the halo. The observations were filled with artifacts and were not usable. We conclude that a deep P-band image with the new correlator of the Jansky VLA is required in order to detect the large faint halo emission. Since the halo flux was undetected, the flux density of the secondary at 1.552 GHz will yield a conservative estimate of the isotropic flux density at 151 MHz. Thus, we choose a steep spectral index of $\alpha = 1$ for the extrapolation to 0.69 Jy of isotropic flux density at 151 MHz. From Equation (10) with $10 < \mathcal{F} < 20$, this equates to an estimate of the long-term time-averaged jet power of $\overline{Q} = (9.81 \pm 3.27) \times 10^{44}$ ergs s^{-1}.

B.4. The Extended Diffuse Flux of 3C 345

A deep L-band VLA image has been previously published (Murphy et al. 1993). However, the data reduction does not separate the isotropic extended flux from the dominant one-sided jet (which is likely beamed). Thus, we use the archival A-configuration observation at 1.552 GHz from 1984 December 23 in order to estimate the isotropic extended flux. The image is restored with a 1.″5 circular beam and is presented in Figure B2.

The total flux density in Figure 12 is 8.934 Jy. The flux density of the (Core + Jet/Northern Hot spot) is 8.639 Jy. The extended isotropic flux density estimated as Total − (Core + Jet/Hot spot) is 0.295 mJy. This is primarily very diffuse halo type emission and is likely very steep spectrum. It is likely that more of this flux would be detected in B and C configurations. Thus, we choose $\alpha = 1$ to extrapolate to the isotropic flux density to 151 MHz. Clearly a much better estimate could be achieved with the aid of a new P-band Jansky VLA image. Based on the current image and data reduction, we find that $F_{151} = 3.03$ Jy. From Equation (10) with $10 < \mathcal{F} < 20$, this equates to an estimate of the long-term time-averaged jet power of $\overline{Q} = (2.59 \pm 0.86) \times 10^{45}$ ergs s^{-1}.

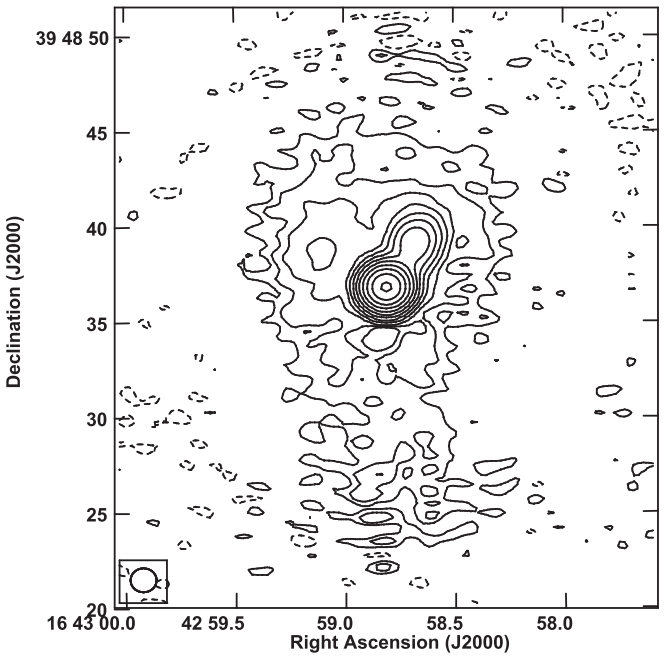

Figure B2. The 1552 MHz image of 3C 345. The radio contours are in percentage of peak surface brightness (=7.7 Jy beam^{-1}) and increase in steps of 2, with the lowest contour being ±0.042%. Note the diffuse halo type emission that surrounds the core−jet structure.

B.5. The Extended Diffuse Flux of 3C 454.3

One object that did not have an existing deep radio image that revealed the diffuse isotropic extended emission is the famous blazar 3C 454.3. Even the excellent observations of Murphy et al. (1993) only reveal a core−jet morphology with the jet directed toward Earth with a strong possibility of significant Doppler beaming on kiloparsec scales (Punsly 1995). In Figure B3, never-before-published images from the VLA in A-configuration observation on 1999 August 10 at L band are presented. We show images at slightly different frequencies (1435 MHz and 1365 MHz), in order to explore possible artifacts in diffuse structure.

Compare the left panel of Figure B3 at 1365 MHz with the right panel. There is a prominent feature to the northeast of the jet terminus that is much weaker in the lower 1435 MHz image. This is considered an artifact. By contrast, the excess emission surrounding the jet terminus that is pronounced toward the east is apparent at both frequencies and is concluded to be inherent to 3C 454.3. We estimate a flux density of 51 mJy at 1.4 GHz for this feature. There is also a feature that protrudes to the west of the core (a possible counterjet) that appears in both images and is likely associated with 3C 454.3. We estimate a flux density of 11 mJy at 1.4 GHz for this feature. The combined extended flux density is 62 mJy at 1.4 GHz. From Equation (10) with $10 < \mathcal{F} < 20$, this equates to an estimate of the long-term time-averaged jet power of $\overline{Q} = (1.36 \pm 0.45) \times 10^{45}$ ergs s^{-1}.

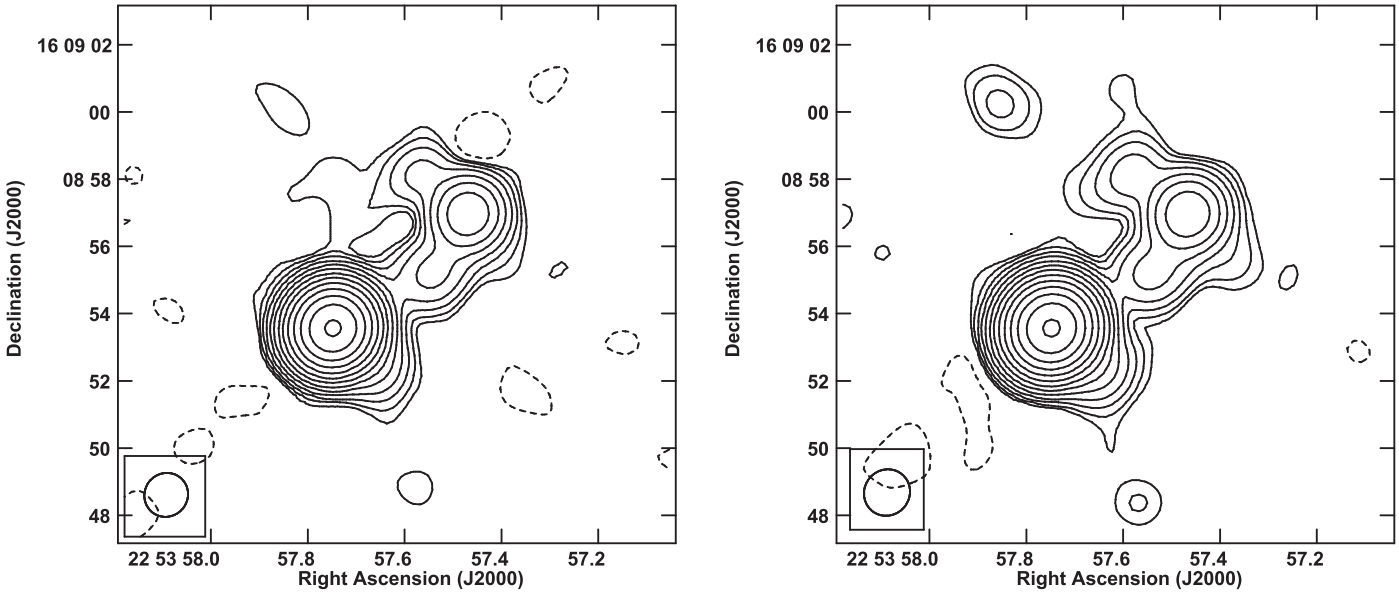

Figure B3. The 1365 MHz (left) and 1435 MHz (right) images of 3C 454.3. The radio contours are in percentage of peak surface brightness (left: 13.35 Jy beam^{-1}; right: 13.32 Jy beam^{-1}) and increase in steps of 2, with the lowest contour being ±0.02%. Comparing the two panels indicates that there is an artifact to the northeast of the hot spot in the left image.

ORCID iDs

Brian Punsly https://orcid.org/0000-0002-9448-2527
Paola Marziani https://orcid.org/0000-0002-6058-4912
Marco Berton https://orcid.org/0000-0002-1058-9109
Preeti Kharb https://orcid.org/0000-0003-3203-1613

References

Aars, C. E., Hough, D. H., Yu, L. H., et al. 2005, AJ, 130, 23
Antonucci, R., & Ulvestad, J. 1985, ApJ, 294, 158
Antonucci, R. J. 1993, ARA&A, 31, 473
Balmaverde, B., & Capetti, A. 2014, A&A, 563, 119
Barthel, P. 1989, ApJ, 336, 606
Barthel, P., Tytler, D., & Thomson, B. 1990, A&AS, 82, 339
Beckmann, V., Soldi, S., Ricci, C., et al. 2009, A&A, 505, 417
Bentz, M., Walsh, B., Barth, A., et al. 2004, ApJ, 705, 199
Berton, M., Liao, N., La Mura, G., et al. 2018, A&A, 614, 148
Best, P., Rottgering, H., & Lehnert, M. 1999, MNRAS, 310, 223
Bicknell, G., Dopita, M., Tsvetanov, Z., & Sutherland, R. 1998, ApJ, 495, 680
Blundell, K., & Rawlings, S. 2000, AJ, 119, 1111
Britzen, S., Krichbaum, T., Strom, R., et al. 2005, A&A, 444, 443
Brotherton, M. 1996, ApJS, 102, 1
Brotherton, M., Wills, B., Steidel, C., & Sargent, W. 1994, ApJ, 430, 131
Bruhweiler, F., & Verner, E. 2008, ApJ, 675, 83
Chen, K., & Halpern, J. P. 1989, ApJ, 344, 115
Clavel, J., Nandra, K., Makino, F., et al. 1992, ApJ, 393, 113
Corbin, M. 1997a, ApJ, 485, 517
Corbin, M. 1997b, ApJS, 113, 245
Corbin, M., & Francis, P. 1994, AJ, 108, 2016
Davis, S., & Laor, A. 2011, ApJ, 728, 98
de Pater, I., & Perley, R. 1983, ApJ, 273, 64
DeCarli, R., Dotti, M., & Treves, A. 2011, MNRAS, 413, 39
Emmering, R., Blandford, R., & Shlosman, I. 1992, ApJ, 385, 460
Evans, I., & Koratkar, A. P. 2004, ApJS, 150, 73
Fanaroff, B. L., & Riley, J. M. 1974, MNRAS, 167, 31P
Fejes, I., Porcas, R., & Akujor, C. 1992, A&A, 257, 459
Ferland, G., Porter, R., van Hoof, P., et al. 2013, RMxAA, 49, 137
Garrington, S., Conway, R., & Leahy, J. 1991, MNRAS, 250, 171
Ghisellini, G., Tavecchio, F., Foschini, L., et al. 2010, MNRAS, 402, 497
Greene, J. E., & Ho, L. C. 2005, ApJ, 630, 122
Gupta, A., Mangalam, A., & Wiita, P. 2017, MNRAS, 472, 788
Hummel, C., Muxlow, T., Krichbaum, T., et al. 1992, A&A, 266, 93
Impey, C., Lawrence, C., & Tapia, S. 1991, ApJ, 375, 46
Impey, C., & Tapia, S. 1990, ApJ, 354, 124
Jackson, N., & Browne, I. W. A. 1991, MNRAS, 250, 422
Jarvis, M., & McLure, R. 2006, MNRAS, 369, 182
Jorstad, S., Marscher, A., Morozova, D., et al. 2007, ApJ, 846, 98
Kellerman, K. I., Lister, M. L., Homan, D. C., et al. 2004, ApJ, 609, 539
Kellermann, K. I., Pauliny-Toth, I. I. K., & Williams, P. J. S. 1969, ApJ, 157, 1
Kharb, P., Lister, M., & Cooper, N. 2010, ApJ, 710, 764
Kinney, A., Bohlin, R., Blades, J., & York, D. 1991, ApJS, 75, 645
Kong, M.-Z., Wu, X.-B., Wang, R., & Han, J.-L. 2006, ChJAA, 6, 396
Korista, K. T., Baldwin, J., Ferland, G., & Verner, D. 1997, ApJS, 108, 401
Laor, A., & Davis, S. 2014, ApJ, 428, 3024
Laor, A., Fiore, F., Elvis, M., Wilkes, B., & McDowell, J. 1997, ApJ, 477, 93
Lawrence, C., Zucker, J. R., Readhead, A. C. S., et al. 1996, ApJS, 107, 541
Leon-Tavares, J., Chavushyan, V., Patino-Alvarez, V., et al. 2013, ApJ, 763, 36
Lightman, A., Press, W., Price, R., & Teukolsky, S. 1975, Problem Book in Relativity and Gravitation (Princeton: Princeton Univ. Press)
Lind, K., & Blandford, R. 1985, ApJ, 295, 358
Lister, M., Aller, M., Aller, H., et al. 2016, AJ, 152, 12
Lister, M. L., Aller, M. F., Aller, H. D., et al. 2013, AJ, 146, 120
Malkan, M. 1983, ApJ, 268, 582
Malkan, M., & Moore, R. 1986, ApJ, 300, 216
Marziani, P., Sulentic, J., Dultzin-Hacyan, D., Calvani, M., & Moles, M. 1996, ApJS, 104, 37
Marziani, P., Sulentic, J., Plauchu-Frayn, I., & del Olmo, A. 2013, A&A, 555, 89
McCarhty, P. 1993, ARA&A, 31, 639
Murphy, D., Browne, I. W. A., & Perley, R. 1993, MNRAS, 264, 298
Netzer, H., Kazanas, D., Baldwin, J., Ferland, G., & Browne, I. W. A. 1995, ApJ, 430, 191
Nilsson, K., Pursimo, T., Villforth, C., Lindfors, E., & Takalo, L. O. 2009, A&A, 505, 601
Pearson, T., & Readhead, A. 1981, ApJ, 248, 61
Peterson, B. M., Ferrarese, L., Gilbert, K., et al. 2004, ApJ, 613, 682
Piconcelli, E., Jimenez-Bailón, E., Guainazzi, M., et al. 2005, A&A, 432, 15
Popovic, L., Vince, I., Atanackkovic-Vukmanovic, O., & Kubicela, A. 1995, A&A, 293, 309
Punsly, B. 1995, AJ, 109, 1555
Punsly, B. 2007, MNRAS, 374, 10
Punsly, B. 2010, ApJ, 713, 232
Punsly, B. 2012, ApJL, 762, 25
Punsly, B. 2014, ApJL, 797, 33
Punsly, B. 2015, ApJ, 806, 47
Punsly, B., & Kharb, P. 2016, ApJ, 833, 57
Punsly, B., & Kharb, P. 2017, MNRAS, 468, 72
Punsly, B., Marziani, P., Zhang, S., Muzahid, S., & O'Dea, C. 2016, ApJ, 830, 104
Punsly, B., & Tingay, S. 2005, ApJL, 633, 89
Punsly, B., Tramacere, P., Kharb, P., & Marziani, P. 2018, ApJ, 869, 164

Punsly, B., & Zhang, S. 2011, ApJL, 735, 3
Reid, A., Shone, D., Akujor, C., et al. 1995, A&AS, 110, 213
Richards, G. T., Vanden Berk, D. E., Reichard, T. A., et al. 2002, AJ, 124, 1
Rumnoe, J., Brotherton, M., Shang, Z., Wills, B., & DiPompeo, M. 2013, MNRAS, 429, 135
Saikia, D., Muxlow, T., & Junor, W. 1990, MNRAS, 245, 503
Scott, J., Kriss, G., Brotherton, M., et al. 2004, ApJ, 615, 135
Shen, Y., & Liu, X. 2012, ApJ, 753, 125
Smith, H., & Spinrad, H. 1980, ApJ, 236, 419
Spinrad, H., Djorgovski, S., Marr, J., & Aguilar, L. 1985, PASP, 97, 932
Steffen, A., Strateva, I., Brandt, W. N., et al. 2006, AJ, 131, 2826
Stevans, M., Shull, M., Danforth, C., & Tilton, E. 2014, ApJ, 794, 75
Sulentic, J., Marziani, P., & Dultzin-Hacyan, D. 2000, ARA& A, 38, 521
Sun, W.-H., & Malkan, M. A. 1989, ApJ, 346, 68
Tang, B., Shang, Z., Gu, Q., Brotherton, M. S., & Runnoe, J. C. 2012, ApJ, 201, 38
Telfer, R., Zheng, W., Kriss, G., & Davidsen, A. 2002, ApJ, 565, 773
Torrealba, J., Chavushyan, V., Cruz-Gonzalez, I., et al. 2012, RMxAA, 48, 9
Trakhtenbrot, B., & Netzer, H. 2012, MNRAS, 427, 3081
Urry, C. M., & Padovani, P. 1995, PASP, 107, 803
van Breugel, W., Miley, G., & Heckman, T. 1984, AJ, 189, 5
Vestergaard, M., & Peterson, B. 2006, ApJ, 641, 689
Vestergaard, M., & Wilkes, B. 2001, ApJS, 134, 1
Walker, R., Benson, J., & Unwin, S. 1987, ApJ, 316, 546
Wandel, A., Peterson, B., & Malkan, M. 1999, ApJ, 526, 579
Wang, J.-M., Luo, B., & Ho, L. 2004, ApJL, 615, 9
Willott, C., Rawlings, S., Blundell, K., & Lacy, M. 1999, MNRAS, 309, 1017
Wills, B., & Brotherton, M. 1995, in Jets from Stars and Galactic Nuclei, ed. W. Kundt, Vol. 471 (Berlin: Springer), 203
Wills, B., Thompson, K., Han, M., et al. 1995, ApJ, 447, 139
Wills, B., Wills, D., Breger, M., Antonucci, R., & Barvainis, R. 1992, ApJ, 398, 454
Wills, B. J., & Browne, I. W. A. 1986, ApJ, 302, 56
Woo, J.-H., Treu, T., Barth, A., et al. 2010, ApJ, 716, 269
Zheng, W., Kriss, G., Telfer, R., et al. 1997, ApJ, 475, 469